Wind Generated Electricity Using Flexible Piezoelectric Materials

A THESIS
SUBMITTED TO THE FACULTY OF THE GRADUATE SCHOOL
OF THE UNIVERSITY OF MINNESOTA
BY

Dustin Lee Morris

IN PARTIAL FULFILLMENT OF THE REQUIREMENTS
FOR THE DEGREE OF
MASTER OF ELECTRICAL ENGINEERING

William P. Robbins

December, 2010

Acknowledgements

Thank you Initiative for Renewable Energy and the Environment (IREE), Excel Energy, and the National Science Foundation for funding this research project.

Thank you Dr. William P. Robbins for offering me this research assistantship. I don't know where I would be without your help, guidance, and most of all patience.

Thank you Dad for pushing me to be the best I can be. You have molded me into the person I am today.

Thank you Uncle Scott and Uncle Stan for convincing me to pursue an Electrical Engineering degree at the University of Minnesota. It has been a wonderful journey thus far.

Thank you Dave and Chrissy for giving me a fun and relaxing Florida vacation in the midst of this research project.

Thank you Brittany for your love and support. Each day is a little brighter with you in it.

And finally, thank you Mom for always believing in me. You have my deepest gratitude for all your love and support.

Dedication

This thesis is dedicated to my Mom, Anne Marie Morris. You are the one who has believed that I could do anything since I was just a boy. Thank you...

Abstract

Wind generated electricity using thin, flexible sheets of piezoelectric materials attached to flag like membranes termed bimorphs is presented. Piezoelectric wind generated electricity presents a simple, yet effective means to extract energy from the environment. The harvested energy would most likely be used to power wireless sensor networks and other low power applications where batteries would normally be used. Replacing batteries is inconvenient for the users of wireless sensor networks and consumers of other low power electronics. Recharging batteries with power extracted directly from the ambient eliminates the need for frequent battery replacement.

Bimorphs are constructed with piezoelectric materials such as poled Polyvinylidene Fluoride (PVDF) and Lead Zirconate Titanate (PZT). Various thin, flexible polymers such as overhead projector film or ink jet transparency film make up the substrate. Several adhesives are researched to determine which can withstand the high strain levels over long periods of time. Bluff bodies were used to create vortex shedding; to increase the undulation amplitude of the bimorph and overall efficiency of the piezoelectric energy harvesting system.

Due to the low source capacitance of piezoelectric materials and the low oscillation frequency of the bimorph, the source impedance is very high. In order to reduce the source impedance of the bimorph (increase output current), an inductor must resonate out some or all of the reactance of the piezoelectric. However, thousands of henries of inductance would be necessary to have a vast impact on piezoelectric source impedance. Hence, a quasi-resonant rectifier switching circuit is employed to reduce the source impedance of the bimorph.

An energy harvesting circuit termed 'Series Synchronized Switch Harvesting on Inductor' (SSSHI) is implemented in order to maximize AC to DC power flow from a piezoelement bimorph to a storage capacitor. The circuit comprises of a peak-triggering circuit, inductor, switch, and regulated micro-power step-down converter powered directly from the piezoelement.

Thesis Supervisor: William P. Robbins

Title: *Wind Generated Electricity Using Flexible Piezoelectric Materials*

Table of Contents

List of Tables

List of Figures

CHAPTER 1

Introduction

The motivation for this thesis work is to provide small amounts of off-grid power for consumer electronic devices, as well as trickle charging batteries. Recent advances in low power electronics have provided new opportunities for the use of piezoelectric materials to power consumer electronic devices; either without the need for batteries, or in conjunction with rechargeable batteries. Typical applications include wireless sensors, wireless networks, wearable computers, cell phones, MP3 players, and other portable electronic devices. All of these systems or devices require power from batteries or some other energy source when not connected to the electric grid.

One solution is to build a better battery. Another solution is energy scavenging from the ambient environment and more specifically, from wind power. By using piezoelectric materials adhered to a substrate (non-active core) that is allowed to undulate or flap in the passing wind; small amounts of power (1-100mW) generation are attainable via the bending of the piezoelement. The bending of the piezoelement gives rise to strains in the piezoelectric which creates an electric field due to direct piezoelectric effect. Commercially available piezoelectric materials such as PVDF and PZT based macro-fiber composites (MFCs) are flexible enough to use in a flag-like structure termed a unimorph, bimorph (doubles-sided) or piezoelement. These piezoelectric materials are very capable of producing usable energy to power many consumer electronic devices as well as wireless sensor networks.

1.1 Background

Previous studies of eel-like membranes of piezoelements used in water flow applications have already explored the feasibility of harnessing energy of turbulent flow. The eel-like membranes consist of a central non-active core and an active piezoelectric material PVDF adhered to each side of the core in a bimorph configuration. Using lengths from 12” to 16”, these eels were used to determine optimal geometries of the eel-like membranes and bluff body to achieve frequency coupling of the eel-like membrane with the Von Kármán vortex street given off by the bluff body [1].

Another article entitled “Energy Harvesting Eel” addresses the feasibility of placing an electric eel in the wake of a bluff body. This research focused on the vortex streets given off by the bluff body. An important conclusion from this work states that frequency coupling may be attained between an eel-like bimorph and a vortex street. This in turn will produce higher power efficiencies [2].

Research involving piezoelectric materials used on the rotors of a wind turbine has previously been done by V. Hugo Schmidt of Montana State University. He has proposed a few designs as well as patents to develop

this concept. His research proposes that it may be feasible to use piezoelectric polymers on a large scale, with a power output density approaching 100W/cm^3 [3].

Other research has focused on a piezoelectric windmill concept at the University of Texas at Arlington. In this research wind flow causes a fan to rotate, and the torque generated from the fan is transferred to an attached wind mill shaft. A cam mounted on the shaft deflects a pre-stressed bimorph pressed against the cam and produces charge through direct piezoelectric effect. In this research 12mW DC power was generated using 11 working bimorphs at a matched load of 4.6kΩ [9].

Wind generated electricity using thin, flexible sheets of piezoelectric material has been previously researched at the University of Minnesota under the direction of Dr. William P. Robbins. In this work, the maximum power generated from a bimorph element undulating in the wind employing a standard full-wave rectifier at matched load was 8.4mW DC power at a wind speed of 15.7m/s.

Piezoelectric materials are intrinsically capacitive. Therefore at low excitation frequencies very low currents are realizable due to their high output impedance. Higher output current and hence more power can be achieved via resonating an inductor with the intrinsic capacitance of the piezoelectric. Due to the fact that the piezoelement frequency of oscillation is 5-10Hz and the capacitance of commercially available piezoelectrics is in the nano/microfarad range, it is physically unrealistic to design an inductor with enough inductance to resonate with the piezoelectric capacitance at the frequency of oscillation.

A Synchronized Switch Harvesting on Inductor (SSHI) circuit is used to provide resonance between an inductor and the intrinsic capacitance of the piezoelectric material. An SSHI circuit has been found to lower the optimum load resistance by a significant amount (factor of four has been demonstrated). Thus, the SSHI circuit can source several times more power than that of a conventional full-wave rectifier. The performance of the SSHI circuit is highly dependent on the Q value of the magnetic components and the switch characteristics.

A piezoelectric energy harvesting circuit has been previously studied by Ottmann [4]. The energy harvesting circuit developed in Ottmann's research has shown that four to five times the maximum output power of a conventional full-wave rectifier can be obtained under ideal conditions. In this research Ottman uses a step-down converter topology with optimized duty cycle to increase electrical energy extraction from the piezoelectric material. A simplified schematic is shown in **Figure 1.1**.

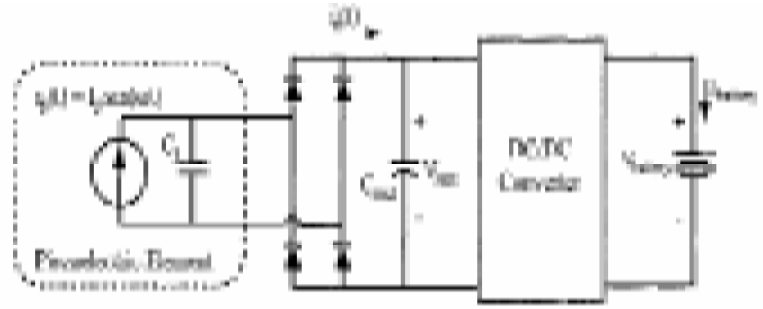

Figure 1.1 *Simplified schematic of energy harvesting circuit used by Ottmann.*

1.2 Objective

The objective for this work is to dramatically increase the mechanical to electrical power conversion efficiency of piezoelectric materials subjected to alternating stresses caused by wind energy. A realistic goal is to increase the efficiency from 0.02% to 0.2%. This will be accomplished by implementing a Series Synchronized Switch Harvesting on Inductor (SSSHI) circuit and employing an optimal geometry of the piezoelement and bluff body.

The SSSHI circuit is to be powered directly from the piezoelement itself. No batteries are needed for initial start-up or to provide a supply voltage to the switching circuit. A micro-power regulated step-down converter is implemented to provide a 3Vdc supply voltage to the SSSHI switching circuit. The step-down converter is optimized to have extremely low power dissipation (less than 1% of additional energy harvested via SSSHI); therefore, switching frequency is minimized in the DC/DC converter design.

The Q value of the inductor has a significant impact on the efficiency of the SSSHI circuit. Therefore, a custom high-Q inductor is designed to maximize SSSHI performance.

1.3 Overview

Chapter 2 discusses the design and electrical characterization of the piezoelement wind-electric generation system concept. It provides a basic introduction of piezoelectric theory and terminology and physical principles involved in bending 31-mode electromechanical transduction. PVDF sheets were chosen for the piezoelectric material of the flag-like membrane due to its flexibility and commercial availability. The piezoelectric flag-like membrane prototype construction is described. An equivalent circuit model is derived for the bimorph.

Chapter 3 gives a brief overview of preliminary experiments as well as initial efficiency estimates. Maximum power measurements are taken for the conventional full-wave rectifier as well as the SSSHI circuit for the PVDF piezoelement.

Chapter 4 describes two methods to increase the electrical energy extraction from the piezoelectric material. The first method used is Series Synchronized Switch Harvesting on Inductor. The second method involves increasing the flapping amplitude of the piezoelement via bluff bodies upwind from the piezoelement as well as adding mass to the free end of the piezoelement.

Chapter 5 explains the operation of the SSSHI circuit including the peak-triggering circuit, switch implementation, and micro-power regulated step-down converter. A specialized inductor is designed for the SSSHI circuit. Analysis and design of the inductor is given.

Chapter 6 states the best results obtained using piezoelectric materials to harvest wind energy in this research. Piezoelement fatigue testing is explored as well.

Chapter 7 discusses future research to further increase wind kinetic energy to DC electrical energy conversion efficiency of the piezoelement.

CHAPTER 2

Piezoelectric Harnessing of Wind Energy Concept

The following chapter develops the concept of extracting electrical energy from wind energy using piezoelectric materials. It begins with an electrical model for the piezoelement, delves into the flag-like membrane structure, provides an overview of piezoelectric materials, and finally discusses the geometry and construction of the piezoelement.

2.1 Electrical Model of the Piezoelement

As a piezoelectric material undergoes an alternating compression/tension cycle it produces a near-sinusoidal voltage across its electrodes due to direct piezoelectric effect. The piezoelectric effect is the transfer of kinetic/mechanical energy to electrical energy. The piezoelectric material behaves like a parallel plate capacitor having a total electrostatic capacitance expressed by Equation 2.1. The capacitance of a unimorph PVDF (8" x 10" x .002") sheet is calculated in Equation 2.2.

$$C_{PVDF} = \varepsilon_0 \varepsilon_R \left(\frac{A}{d} \right) \qquad \text{(Equation 2.1)}$$

$$C_{PVDF} = (8.85x10^{-12} F/M)(11)\left(\frac{513cm^2}{.005cm} \right) = 100nF \qquad \text{(Equation 2.2)}$$

In Equation 2.1 ε_o is the permittivity of free space, ε_r is the relative permittivity of PVDF, 'A' is the electrode area, and 'd' is the thickness of the PVDF. Given these facts, a piezoelectric transducer under constant amplitude, alternating stress can be modeled as an alternating voltage source in series with a capacitance as shown in **Figure 2.1**.

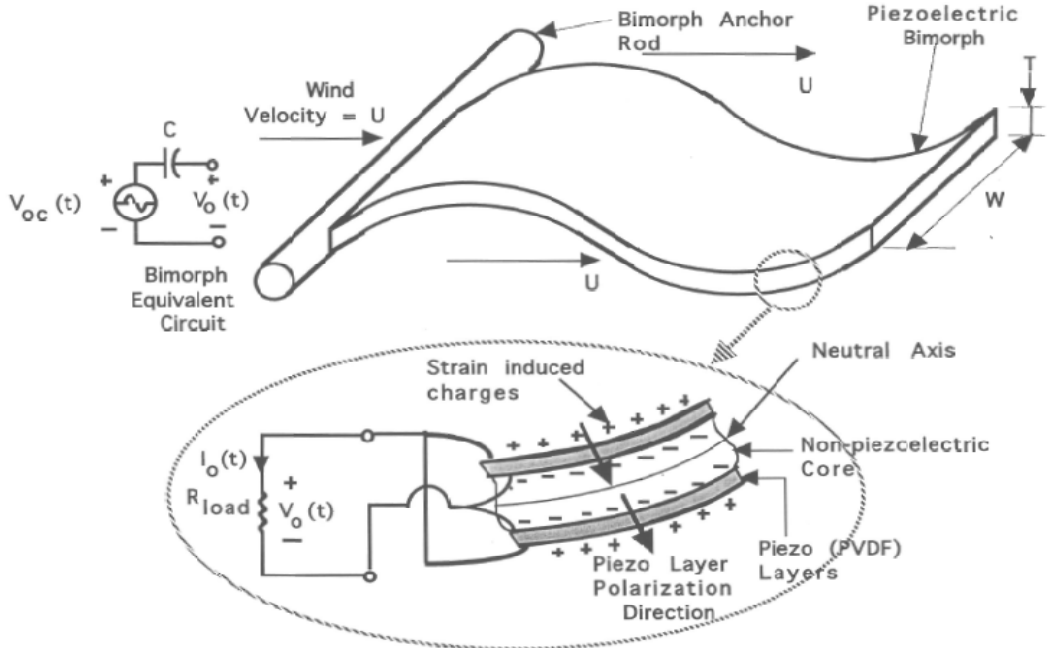

Figure 2.1 *Proposed concept for wind-generated electric power using piezoelectric materials. In the equivalent circuit, C is the electrostatic capacitance of the bimorph and $V_{oc}(t)$ is the open circuit voltage generated by the undulation of the bimorph subjecting strains on the piezoelement* [5].

Also shown in the **Figure 2.1** a bimorph consists of two piezoelectric layers; one on the top surface of the non-active core and one on the bottom surface. Each PVDF sheet is electrically in parallel, therefore the capacitance of each individual sheet can be summed together to give a total capacitance 'C' of the bimorph. The open-circuit voltage remains the same due to the fact that the same amount of strain is applied to both piezo layers and each layer has the same piezoelectric constant. Therefore, a periodic voltage (with magnitude of the piezoelectric open-circuit voltage) in series with the combined capacitance of each layer completes the piezoelement electrical circuit model.

If multiple piezoelements are oscillating in a synchronous fashion, the complete system can be modeled as a single voltage source in series with a total combined capacitance equal to the sum of the individual capacitances of each individual piezoelement. The total power is scaled up proportionally by the number of piezoelements added to the system. The multi-piezoelement system concept is shown in the **Figure 2.2**.

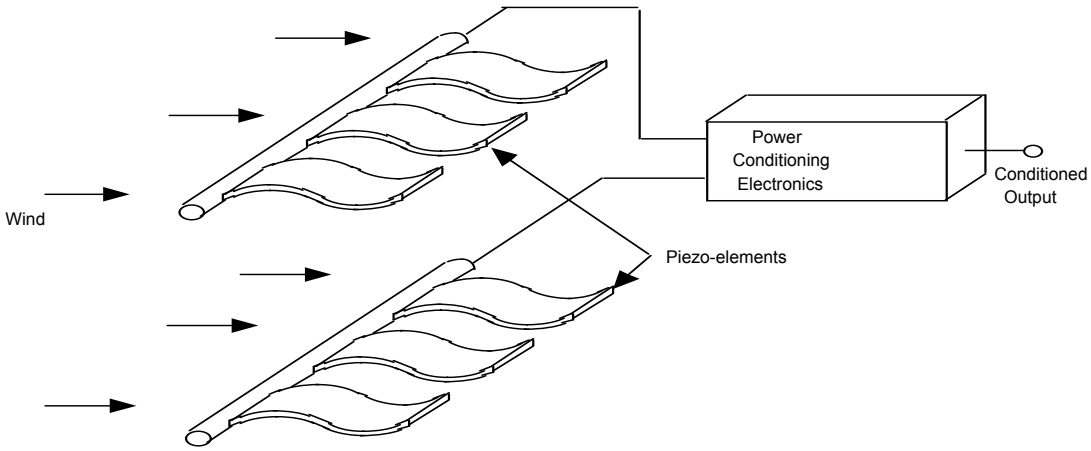

Figure 2.2 *System concept for a scalable wind-to-electric conversion system based on the use of piezoelectric materials. The power conditioning electronics would provide power matched to the load requirements such as either DC (for example to charge batteries) or 60Hz AC* [5].

Synchronization of the piezoelements is crucial to overall simplicity of the power conditioning electronics. If the piezoelements oscillate at different frequencies or even out of phase for that matter, power conditioning electronics must be specific to each piezoelement due to the continuous variation of phase difference between piezoelement voltage peaks (explained further in **Chapter 4**). Thus, much more circuitry will be needed for the complete system, greatly increasing the cost of the system design. The synchronization of multiple piezoelements remains an item for further research.

2.2. Piezoelectric Electro-Mechanical Properties

There are two commercially available piezoelectric materials studied in this project, PVDF and MFC (macro-fiber composite)-PZT. PVDF is far more flexible than PZT, whereas PZT has a much higher piezoelectric coefficient than PVDF. MFC-PZT consists of PZT fibers (approximately 200μm in diameter) and several mm long arranged in parallel to each other as a mat-like structure. The PZT fiber mat is sandwiched between layers of adhesive and electrode polyimide film. There are two readily available modes of MFC-PZT, namely d_{31}-mode and d_{33}-mode. D_{31}-mode signifies a mechanical strain perpendicular to the applied voltage direction. A diagram of a macro fiber composite (d33-mode) is shown in **Figure 2.3**.

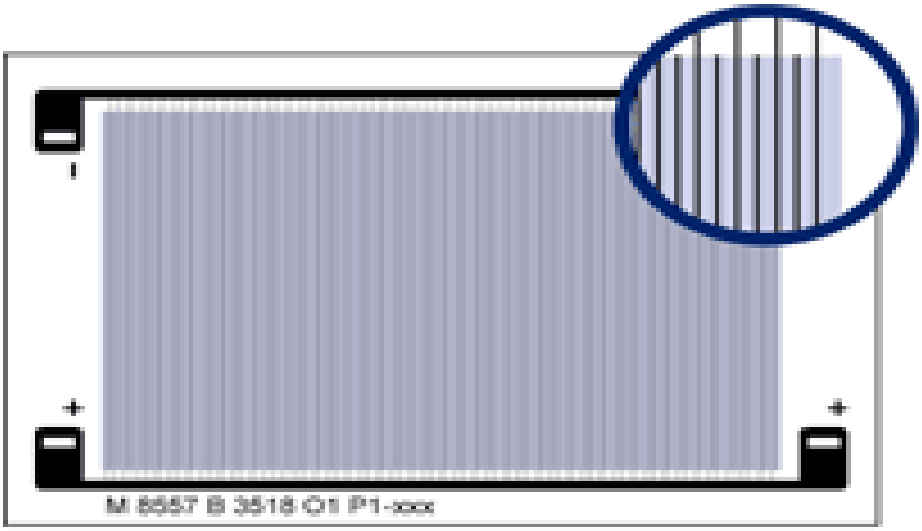

Figure 2.3 *Diagram of Smart Material™ d33-mode MFC-PZT* [10].

A photograph of a macro fiber composite with lateral contracting motion (d31-mode) is shown in **Figure 2.4**.

Figure 2.4 *Photograph of Smart Material™ MFC-PZT with d31 effect* [10].

D_{33}-mode signifies a mechanical strain in parallel with the applied voltage. Although the coupling coefficient of d_{33}-MFC-PZT is approximately twice that of than d_{31}-MFC-PZT, the use of d_{33}-MFC-PCT does not necessarily result in better performance. The electrode structure of both types of MFCs is shown in **Figure 2.5**.

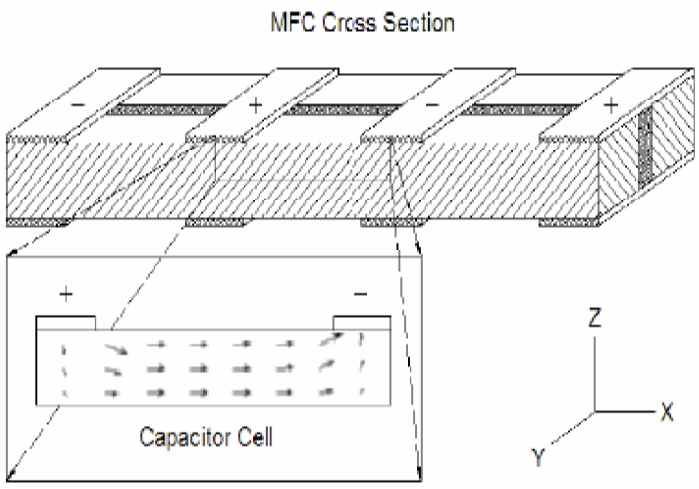

Figure 2.5 *MFC cross section showing capacitance cell of each piezo-finger* [11].

D_{31}-mode MFC-PZT has a much higher capacitance per unit area than d_{13}-mode MFC-PZT because the electrode fingers are located closer together yielding a low open-circuit voltage for a given strain (20-50V). D_{33}-mode MFC-PZT has a lower capacitance than d_{31}-mode MFC-PZT because the fingers are placed farther apart yielding a larger open-circuit voltage for the same applied strain as the d_{31}-mode MFC-PZT (50-300Vpp). A diagram showing the different piezoelectric modes is shown in **Figure 2.6**.

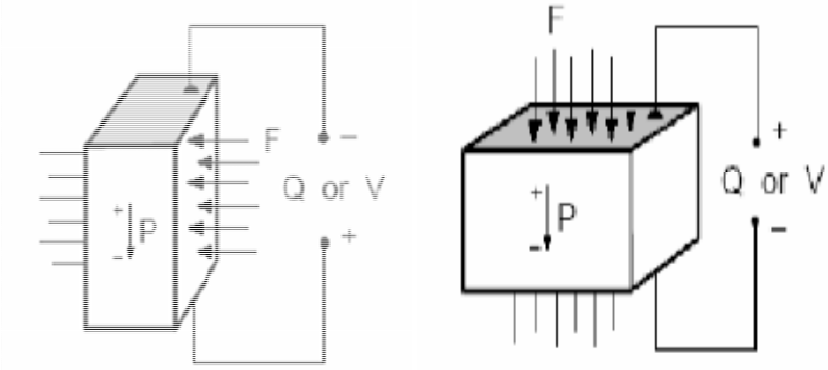

Figure 2.6 *Typical operating modes: d31 (left) and d33 (right)* [11].

The layer capacitance of the d_{31}-mode more than compensates for the smaller voltage compared to the d_{33}-mode. The smaller source impedance of the d_{31}-mode means it can deliver the same or more power to a load than the d_{33}-mode. Performance characteristics for both PVDF and MFC-PZT piezoelectrics are displayed in **Table 2.1**.

Parameter	**PVDF [5]**	**PZT-based MFC [5]**
D_{ij} [C/N]	2.3×10^{-11}	1.70×10^{-10}
Y [N/m^2]	3×10^{9}	3×10^{10}
$\varepsilon_{33}/\varepsilon_o$	12	3000
K_{ij} [J/m^3]	4×10^{7}	10^{9}

Table 2.1 *Electro-mechanical comparison between PVDF-based piezoelement and MFC (PZT)-based piezoelement.*

Among the different types of piezoelectric ceramics, PZT has attracted a great deal of attention, because it has excellent electromechanical properties, such as a high piezoelectric constant (K_{ij}) and a high electromechanical coupling coefficient (D_{ij}) [8]. This is shown in **Appendix A** in equation A11, which is shown below for convenience.

$$P_{\max} = \frac{(d_{ij}Y)^2}{\varepsilon_{ij}}[f_s(LWT)\delta^2] \qquad \text{(A11)}$$

$$P_{\max} = K_{ij}[f_s(LWT)\delta^2] \qquad \text{(Equation 2.3)}$$

Where,

$$K_{ij} = \frac{(d_{ij}Y)^2}{\varepsilon_{ij}} \qquad \text{(Equation 2.4)}$$

Equation 2.3 shows that the maximum available power is directly proportional to the piezoelectric constant (K_{ij}). As shown in **Table 2.1**, MFC-PZT has a piezoelectric constant of 10^9 and PVDF has a piezoelectric constant of 4×10^7. Therefore, theoretically MFC-PZT will have a power density that is 25 times that of PVDF. A diagram of an active fiber composite (d_{33}-mode) is shown in **Figure 2.7**. **Figure 2.8** illustrates

the higher piezoelectric effect of MFC-PZT d_{33}-mode (longitudinal mode) compared to d_{31}-mode (transverse mode).

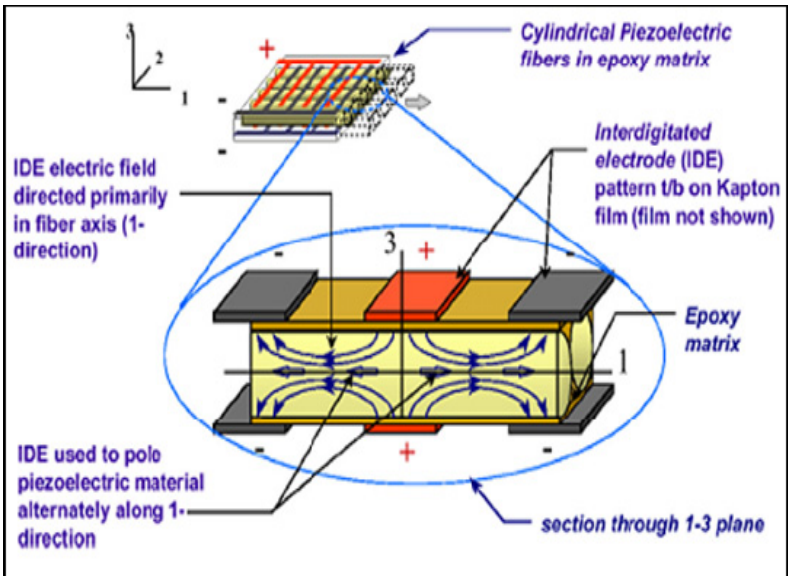

Figure 2.7 *Schematic of active fiber composite (AFC) under d_{33}-mode. D_{33}-mode signifies that the poling axis is in line with the axis under strain* [6].

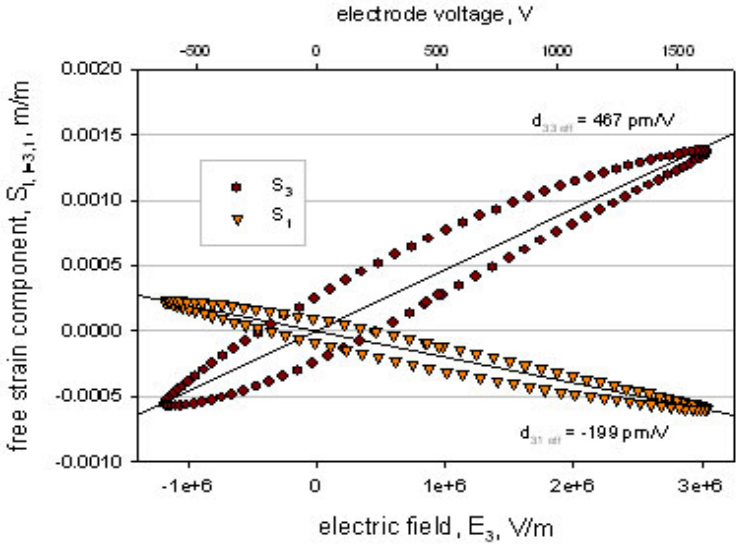

Figure 2.8 *Free Strain d_{31} (S1) and d_{33} (S3) MFCs vs. Electric Field* [10]

Figure 2.8 exemplifies that d_{33}-mode will give over 2.5 times as much voltage as d_{31}-mode. Again, this doesn't necessarily mean the d_{33}-mode will output more power for a given strain. The output power is proportional to the voltage squared multiplied by the capacitance of the MFC. Another point to consider is the high voltages given by the d_{33}-mode will lead to higher voltage rated switches and undoubtedly more losses.

2.3 The Piezoelectric Flag-like Membrane

The initial flag-like membrane dimensions chosen for this research were 8" wide and 11" long. These dimensions were chosen to encompass the PVDF sheet as well as to cover enough area to capture a sufficient amount of wind energy. The substrate was constructed using a plastic polymer with a Young's Modulus on the order of that of PVDF so that the flexibility of the piezoelement is not hampered by the substrate and moderate straining of PVDF/PZT was attainable.

If the stiffness of the substrate is stiffer than the PVDF itself, much of the mechanical energy will be lost in the substrate and not transferred through the piezoelement to provide strains across the PVDF sheet. The initial substrate thickness was chosen to be approximately 500μm. This is thick enough to give moderate strain levels, yet flexible enough to undulate at modest wind speeds (10-15mph). Assuming a uniform airflow, any curvature in the plate will give rise to pressure gradients leading to lift and suction in areas of curvature. Because the plate is flexible, stresses will cause curvatures throughout piezoelement. At high wind speeds the Kelvin-Helmholtz instability will be reached and oscillations will take over. This is shown in **Figure 2.9** [5].

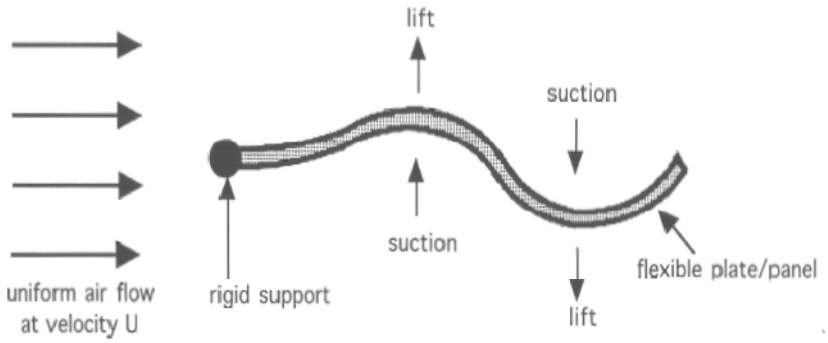

Figure 2.9 *Physical Origin of Flapping – Kelvin-Helmholtz Instability*

The required wind speed U_C to reach the Kelvin-Helmholtz instability is expressed by Equation 2.4, where 't' is the thickness of the PVDF, 'L' is the length of the PVDF, 'Y' is the Young's modulus of PVDF and 'ρ' is the density of air [5].

$$U_C = 2.05\left(\frac{t}{L}\right)\sqrt{Y/\rho} \qquad \text{(Equation 2.4)}$$

The parameters of Equation 2.4 are shown in **Figure 2.10** [5].

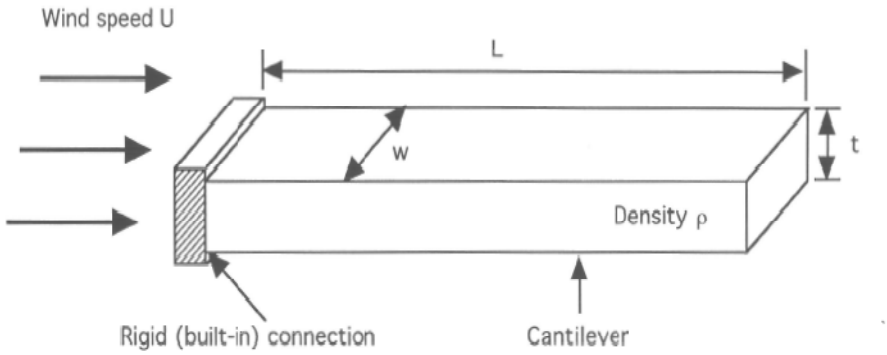

Figure 2.10 *Cantilever beam model.*

The required wind speed (using beam theory) to achieve the Kelvin-Helmholtz instability for the PVDF piezoelement as calculated in Equation 2.5 is 5.3m/s (11.6mph).

$$U_C = 2.05\left(\frac{500\mu m}{25cm}\right)\sqrt{\frac{3GPa}{1.8kg/m^3}} = 5.3m/s \qquad \text{(Equation 2.5)}$$

The actual wind speed needed to achieve bimorph oscillation was found to be approximately 5.94m/s (12mph). The bimorph frequency of vibration is expressed by Equation 2.6 [5].

$$f_c = \frac{U_c}{\pi L} \qquad \text{(Equation 2.6)}$$

The frequency of vibration for the PVDF piezoelement as calculated in Equation 2.7 is 6.75Hz.

$$f_c = \frac{5.3m/s}{\pi(.25m)} = 6.75Hz \qquad \text{(Equation 2.7)}$$

The theoretical frequency of vibration is approximately equal to experimental results which have shown an oscillation frequency close to 7Hz. The bimorph open-circuit output voltage is shown in **Figure 2.11.**

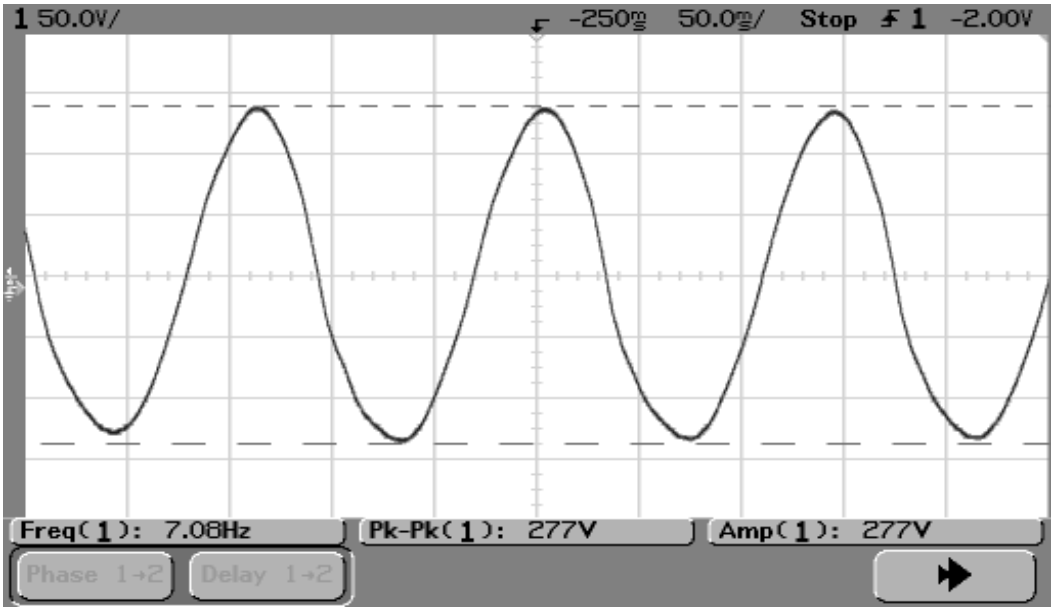

Figure 2.11 *Open-Circuit output voltage waveform of PVDF bimorph (half-sheet of PVDF attached to each side of substrate) flapping in a wind speed of 18mph (8 m/s). Please note a wind speed of 18mph is not necessary to begin oscillations, but was employed here to show high peak-to-peak output voltage.*

As seen in **Figure 2.11** the open-circuit output voltage of the PVDF bimorph is approximately $270V_{pp}$ with little variation. The same open-circuit output voltage is achieved with a PVDF unimorph (one sheet of PVDF attached to substrate). The optimum load resistance will drop by a factor of two with the bimorph, giving rise to twice the output power capacity.

The PVDF output voltage waveform is sinusoidal with nearly constant amplitude. The constant amplitude and stable frequency of oscillation simplifies the peak triggering circuit considerably. A non-sinusoidal, frequency varying voltage waveform requires more complex peak triggering circuitry and hence more power dissipation in the peak-triggering circuit. Therefore, it is vital to build the piezoelement as careful as

possible to achieve sinusoidal oscillation. This includes proper adhesion to ensure no bubbles are formed in the PVDF and solid connections from the PVDF electrodes to the energy harvesting circuitry.

The placement of the electrical output leads on the piezoelement is extremely important to accomplish a sinusoidal signal with little noise (no bumps or spikes). An electrically conductive polymer 3M tape was used to connect the electrical lead wires (AWG30) to the electrically conductive paint (electrodes) of the PVDF. The electrical leads are attached close to the clamped end of the piezoelement to ensure that they are not twisted back and forth during piezoelement bending.

2.3.1 Bimorph Construction

The construction of the flag-like membrane involves attaching the piezoelectric material to the substrate and attaching the substrate to the bluff body. The substrate was constructed using thin overhead projector transparency films. Each transparency film is approximately 3.5mils thick. In order to achieve the desired 19mils or 500µm bimorph thickness, three sheets of transparency film are adhered together to form the substrate. The PVDF to substrate adhesive encompasses the rest of the substrate thickness (~10mils).

Once the substrate is constructed, PVDF is adhered to each side of the substrate with 3M adhesive transfer tape 468MP (with 200MP adhesive). The adhesive transfer tape is approximately 5mils thick and has a trivial effect on the flexibility of the piezoelement. The PVDF sheet is 50µm thick with 10µm electrode paint on each side of the PVDF.

2.3.2 Wind Tunnel Testing

The wind tunnel used in Dr. Robbins's lab within the Electrical and Computer Engineering (ECE) department allows for wind speeds of up to 25mph. The opening of the wind tunnel is approximately 14" x 14". As a means to hold the flag-like membrane in the opening of the wind tunnel, it was connected to a piece of 14" long, 2" diameter PVC pipe. The PVC pipe acts as a bluff body, but more importantly, clamps one end of the flag-like membrane in place so the other end can move freely in the wind. The wind tunnel is shown in **Figure 2.12**.

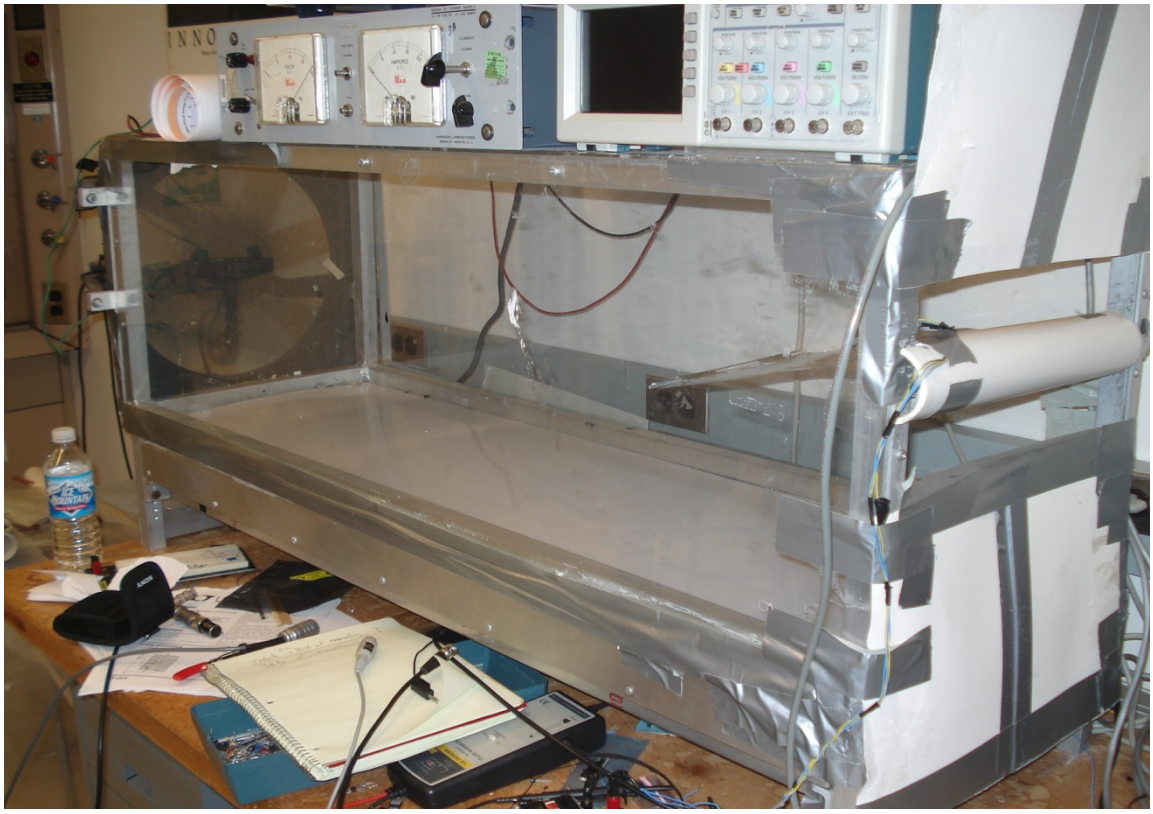

Figure 2.12 *Photograph of the suction wind-tunnel in Dr. Robbins' lab at the Electrical and Computer Engineering (ECE) Department at the University of Minnesota. Blocking pieces of cardboard are placed at wind-tunnel opening to generate higher wind speeds at the bimorph.*

A wind tunnel located in the Aerospace Engineering and Mechanics (AEM) department at the University of Minnesota was also used for testing. The AEM wind tunnel allows for wind speeds up to 40mph. The opening of the wind tunnel is approximately 1' high and 4' wide. In this experiment a 4' long, 2" diameter PVC pipe was used to hold one end of the flag-like membrane and act as a bluff body, as the other end was allowed to flutter freely in the wind. A photograph of the wind tunnel is shown in **Figure 2.13**.

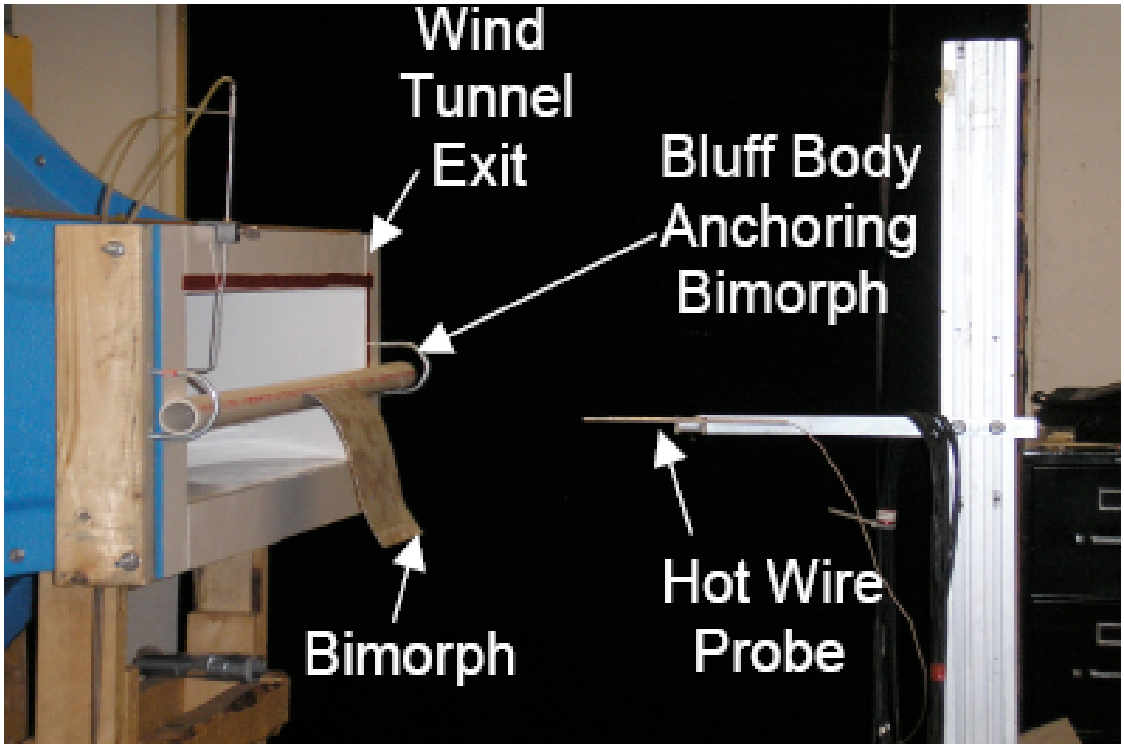

Figure 2.13 *Photograph of wind tunnel and testing setup in the Aerospace Department at the University of Minnesota. The hot wire probe interfaced to a laptop computer using LabView software records wind speeds and vortex frequencies. A digital high-speed camera (Photron, not shown) records the detailed movements of the piezoelement* [5].

Because the height or diameter of the PVC pipes is on the order of 2", there is a trivial amount of frequency coupling between vortex streets given off by the bluff body with the mechanical vibrations of the flag-like membrane. The vortex shedding frequency is expressed by Equation 2.8, where 'Vel' is wind speed and 'D' is the diameter of the PVC pipe [2].

$$f_{strodal} = .2\left(\frac{Vel}{D}\right) = (.2)\frac{(5m/s)}{(.05m)} = 20Hz \qquad \text{(Equation 2.8)}$$

Equation 2.8 shows that a 2" diameter PVC pipe will have a vortex street frequency of 20Hz at a wind velocity of 5m/s. This is much greater than the piezoelement oscillation frequency of 7Hz, hence there is very little frequency coupling between the piezoelement and vortex street given off by the bluff body (PVC pipe). The opening of the AEM wind tunnel is approximately 1 foot as stated earlier. If one were to attempt to use a bluff body on the order of 20cm, there would be very little room for the wind to flow past the bluff body and out of the wind tunnel due to the limited height of the wind tunnel opening. The small passage of

wind flow between the wind-tunnel opening and the bluff body would give rise to an unrealistic testing environment. Therefore bluff bodies greater than four inches in diameter were not used for testing. In further research a wind tunnel with a larger opening will be used to experiment with piezoelement/vortex shedding frequency coupling.

CHAPTER 3

Initial Experiments and Efficiency Estimates

The following chapter provides initial power calculations and efficiency estimates of the piezoelement. Efficiency estimates are based on an approximation of the area of wind that the piezoelement encompasses as it undulates.

3.1 Initial Maximum Power

Initial experiments for this research showed that a bimorph PVDF piezoelement (10" X 8" X .019") could provide 3mW of DC power at a wind speed of 16mph employing a conventional full-wave rectifier. The same bimorph PVDF piezoelement provided 8mW of DC power at a wind speed of 16 mph employing SSSHI.

3.2 Initial Efficiency Estimates

The overall efficiency of the system is expressed in Equation 3.1, where 'P' is the electrical DC power out, 'U' is the wind velocity, ρ_d is the air density, 'A' is the effective wind energy capture area of the piezoelement, E_{f1} is the aerodynamic efficiency of the piezo element (mechanical/elastic energy stored in the piezoelement divided by the input wind energy), E_{f2} is the efficiency of the piezoelectric material in converting stored mechanical/elastic energy into stored electrical energy, and E_{f3} is the efficiency of extracting electrical energy from the piezoelement and delivering it to a load [5].

$$E_f = \frac{P}{\rho_d U^3 A/2} = E_{f1}E_{f2}E_{f3} \qquad \text{(Equation 3.1)}$$

For our preliminary results we estimated E_{f1} to be in the range from 10% to 20% and E_{f2} and E_{f3} to be 10%. The uncertainty in the E_{f1} estimate is due to the difficulty in estimating the effective wind energy capture area of the piezoelement. If the physical area of the unimorph (80 inches^2 or about 0.05 m^2) is assumed for the wind capture area, the overall efficiency of the initial full-wave rectifier experiment is roughly 0.027%. Efficiency derivations are shown below.

$$E_f = \frac{P_{electrical}}{P_{wind}} \quad \text{(Equation 3.2)}$$

$$P_{wind} = \rho V^3 (A/2) = 1.2(7.15m/s)^3 (.025m^2) = 11\text{watts} \quad \text{(Equation 3.3)}$$

Where ρ is air density, V is air velocity, and A is wind energy capture area. Capture area is estimated to be half the piezoelement sheet area (8in x 10in = 80in^2).

Wind energy capture area estimate is based on the average actual motion of the fluttering piezoelement as seen in the wind tunnel. These photographs are shown in **Figure 3.1**.

Figure 3.1. *Photograph of PVDF down stroke (left) and upstroke (right)* [5].

$$E_{f\_FW} = \frac{3mW}{P_{wind}} = \frac{3mW}{11W} = .027\% \quad \text{(Equation 3.4)}$$

$$E_{f\_SSHI} = \frac{8mW}{P_{wind}} = \frac{8mW}{11W} = .073\% \quad \text{(Equation 3.5)}$$

The total energy conversion efficiency from wind energy to DC electrical energy using SSSHI is 0.073%. This total efficiency is a combination of three energy conversions: wind energy to stored elastic energy, elastic energy to stored electrical energy, and stored electrical energy to supplied DC electrical energy. The efficiency of each stage has an equal impact on extractable DC output power. Therefore, each conversion efficiency must be calculated to determine if that stage's efficiency can be increased and by how much. This is very important in realizing a high efficiency power conversion system.

3.2.1 Wind Energy to Elastic Energy Conversion Efficiency

Wind energy available to the piezoelement is approximately 0.77J at a wind speed of 16mph (7.15m/s). Derivation is shown below.

$$E_{wind} = \frac{\rho V^2}{2}\left(A_{eff}\right) = \frac{1.2}{2}(7.15m/s)^2 \times 0.025m^2 = 0.77\ \text{J} \qquad \text{(Equation 3.6)}$$

Elastic energy stored in the PVDF bimorph is approximately 160mJ. Derivation is shown below.

$$E_{mech} = A\int_{t/2-h}^{t/2} Y\left(\frac{2y\varsigma_p}{t}\right)^2 dy = A\left|\frac{4Y\varsigma_p^2}{t^2}\left(\frac{y^3}{3}\right)\right|_{\eta t/2}^{t/2} = A\frac{4Y\varsigma_p^2}{3t^2}\left(\frac{t^3}{8}-\frac{\eta^3 t^3}{8}\right) \qquad \text{(Equation 3.7)}$$

Where $\eta = (t/2-h)*2/t$, where t is the thickness of the piezoelement substrate, h is the thickness of the PVDF, Y is Young's modulus, A is piezoelectric surface area, and ζ_p is the peak strain. Open circuit voltage measurements estimate peak strain to be approximately 0.6% (Voc = 160V).

$$\eta = \left(1-\frac{h}{t/2}\right) = \left(1-\frac{500\mu m}{50\mu/2}\right) = 0.8 \qquad \text{(Equation 3.8)}$$

Equation 3.9 is equation 3.7 simplified.

$$E_{mech} = \left(\frac{AY\varsigma_p^2 t}{6}\right)\left(1-\eta^3\right) \sim \frac{(.05)(3x10^9)(.006)^2(5.0x10^{-4})}{6}(.5) = 230\text{mJ} \qquad \text{(Equation 3.9)}$$

$$E_{f1} = \frac{E_{mech}}{E_{wind}} = \frac{230mJ}{770mJ} = 29.9\% \quad \text{(Equation 3.10)}$$

3.2.2 Stored Elastic Energy to Stored Electrical Energy Conversion Efficiency

The stored electrical energy in the PVDF is in the form of a capacitor where the amount of energy available is given by Equation 3.11. 'C' is the PVDF capacitance, V_{OC} is PVDF open-circuit voltage, ε_{33} is the electrical permittivity of PVDF in the direction of strain and poling, 'A' is the PVDF surface area, and 'h' is the thickness of the PVDF.

$$E_{elec\_stored} = \frac{CV_{oc}^2}{2} \quad \text{(Equation 3.11)}$$

$$C_{PVDF} = \frac{\varepsilon_{33} A_{PVDF}}{h} \quad \text{(Equation 3.12)}$$

From **Appendix A**, the PVDF open-circuit voltage can be expressed as Equation 3.13.

$$V_{oc} = \frac{d_{13} Y h \varsigma_p}{\varepsilon_{33}} \quad \text{(Equation 3.13)}$$

Substituting Equations 3.12 and 3.13 into Equation 3.11, gives us Equation 3.14.

$$E_{elec} = \frac{(d_{13}Y)^2}{2\varepsilon_{33}} h \varsigma_p^2 A_{PVDF} = \frac{\left((2.3x10^{-11})(3x10^{9})\right)^2}{2(12)(8.85x10^{-12})} (50\mu m)(0.006)^2 (0.05m^2) \quad \text{(Equation 3.14)}$$

$$E_{elec} = 2.0\text{mJ} \quad \text{(Equation 3.15)}$$

This gives a stored elastic energy to stored electrical energy conversion efficiency stated by Equation 3.16.

$$E_{f2} = \frac{E_{elec\_stored}}{E_{mech}} = \sim \frac{2.0mJ}{230mJ} = 0.870\% \quad \text{(Equation 3.16)}$$

3.2.3 Stored Electrical Energy to Supplied DC Electrical Energy Conversion Efficiency

Stored electrical energy is calculated below. Frequency in Equation 3.17 is the oscillation frequency of the piezoelement.

$$P_{elec\_stored} = E_{elec\_stored} \times frequency = (2.0mJ)(6Hz) = 12.0mW \quad \text{(Equation 3.17)}$$

This gives an electrical conversion efficiency of 25% for the full-wave rectifier energy extraction and roughly 67% for the SSSHI energy extraction.

$$E_{f3\_FWR} = \frac{P_{electrical\_FWR}}{P_{electrical\_stored}} = \frac{3.0mW}{12.0mW} = 25\% \quad \text{(Equation 3.18)}$$

$$E_{f3\_SSSHI} = \frac{P_{electrical\_SSSHI}}{P_{electrical\_stored}} = \frac{8.0mW}{12.0mW} = 66.7\% \quad \text{(Equation 3.19)}$$

These efficiency estimates show that PVDF will never be a highly efficient energy harvester due to its mechanical to electrical inefficiencies. However, the PVDF piezo-wind harvester system can be further improved with better piezoelement construction, use of bluff bodies and electrical extraction techniques (SSSHI).

CHAPTER 4

Increasing System Efficiency

The following chapter will discuss several techniques used to increase the mechanical to electrical power efficiency of the wind energy piezoelectric system beginning with various methods of increasing the undulation amplitude of the piezoelement. The output voltage of the piezoelectric is directly proportional to the strain across the piezoelectric. Output power is proportional to the square of the voltage. Therefore, it is extremely advantageous to maximize the peak strain of the piezoelement. Finally, this chapter discusses a means to increase the electrical efficiency of AC to DC power transfer using SSSHI.

4.1 Increasing the Undulation Amplitude of the Piezoelement

4.1.1 Adding Mass to the Bimorph Free End

A very simple way to increase the undulation amplitude of the piezoelement is by adding mass to the free end. An experiment varying the amount of added mass to the bimorph free end was conducted in order to maximize output power for a given wind speed. A graph of output power and oscillation frequency as a function of added mass to the free end of the piezoelement is shown in **Figure 4.1**.

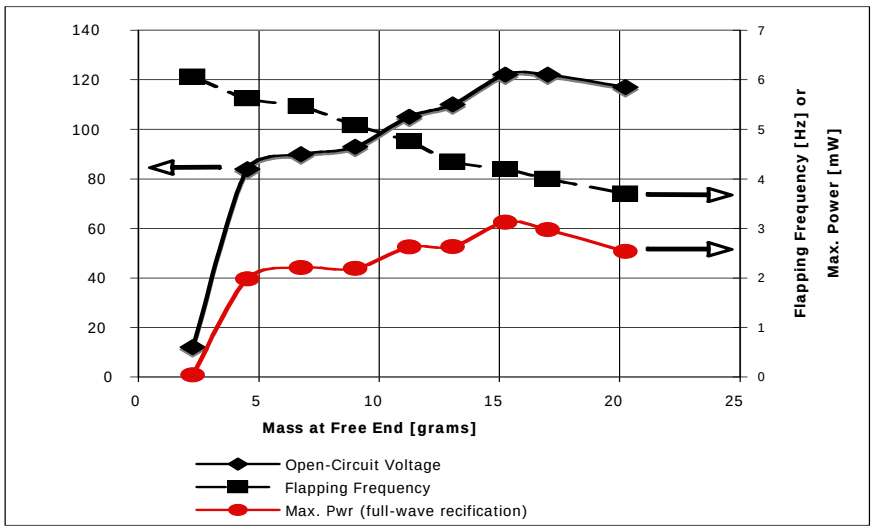

Figure 4.1 *Effect of adding mass to the free end of a flapping piezoelement with PVDF at a wind speed of 15 mph* [5].

The graph of **Figure 4.1** shows that as added mass increases, the open-circuit voltage increases and frequency of oscillation decreases. This is due to the larger oscillation amplitude of the piezoelement which gives rise to more strain and hence greater output voltage. The output power is proportional to the open-

circuit voltage squared multiplied by the oscillation frequency. However, the frequency of oscillation decreases with increasing mass similar to the resonant frequency of a spring-mass system. Therefore, there is a point of negative returns, and an optimum output power will be reached at a specific added mass value.

The optimum added mass to the free end of the piezoelement was empirically found to be approximately 15 grams for a PVDF piezoelement which has dimensions 11" x 8" x .019". The initial mass of the PVDF piezoelement is approximately 60 grams before any additional mass is attached. A photograph of the added mass to the piezoelement can be seen in **Figure 4.2**.

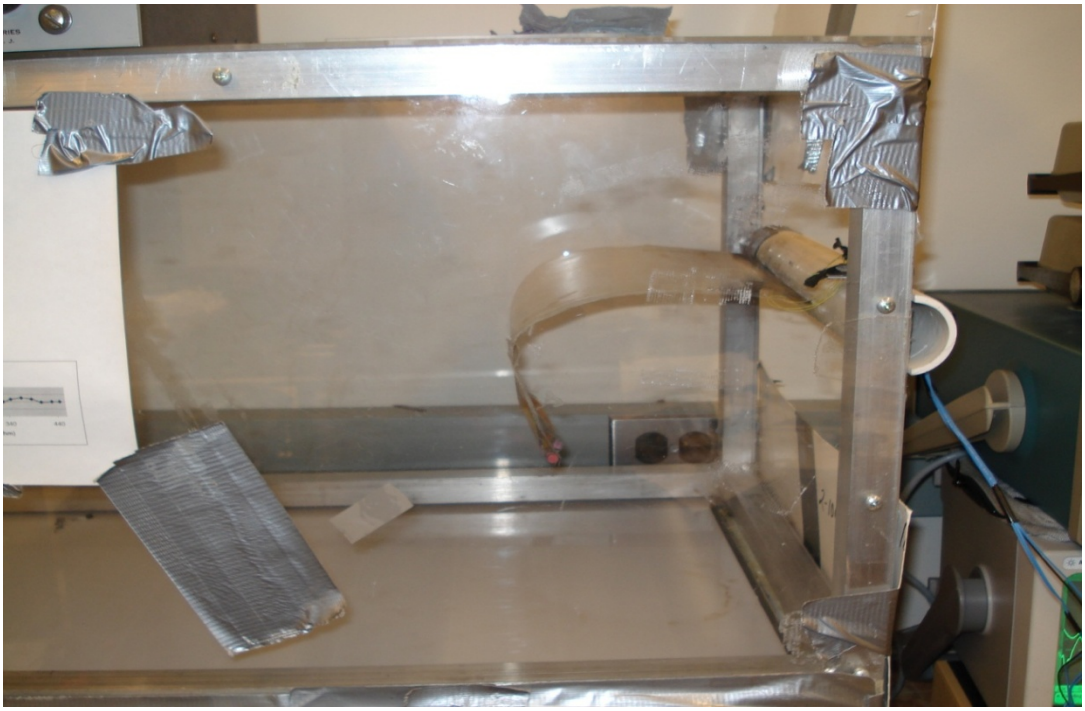

Figure 4.2 *Photograph of PVDF down stroke when mass is added to the free end of the piezoelement (in this case a No. 2 pencil). The added mass greatly increases the curvature of the piezoelement, hence increasing the strain and output voltage of the PVDF as expressed in* ***Appendix A*** *[5].*

4.1.2 Use of a Bluff Body to Increase Undulation Amplitude

Initial use of bluff body experiments showed that the diameter of the bluff body (1 – 4") does not influence the undulation amplitude of the piezoelement due to the fact that the shedding frequency of the vortex street is much higher than the frequency of oscillation of the piezoelement. In order to achieve vortex

street/piezoelement frequency coupling, the height of the bluff body must be on the order of 20cm for a 5m/s wind speed and a piezoelement vibration frequency of 5Hz. This is expressed by Equation 4.1, where V is the wind velocity in m/s, D is the diameter of the cylindrical bluff body in cm, and f is the frequency of vibration in Hz [2].

$$D = 20\left(\frac{V}{f}\right) \qquad \text{(Equation 4.1)}$$

$$D = 20\left(\frac{5m/s}{5Hz}\right) = 20\text{cm} \qquad \text{(Equation 4.2)}$$

A diagram showing the bluff body placed upstream from the piezoelement is displayed in **Figure 4.3** [5].

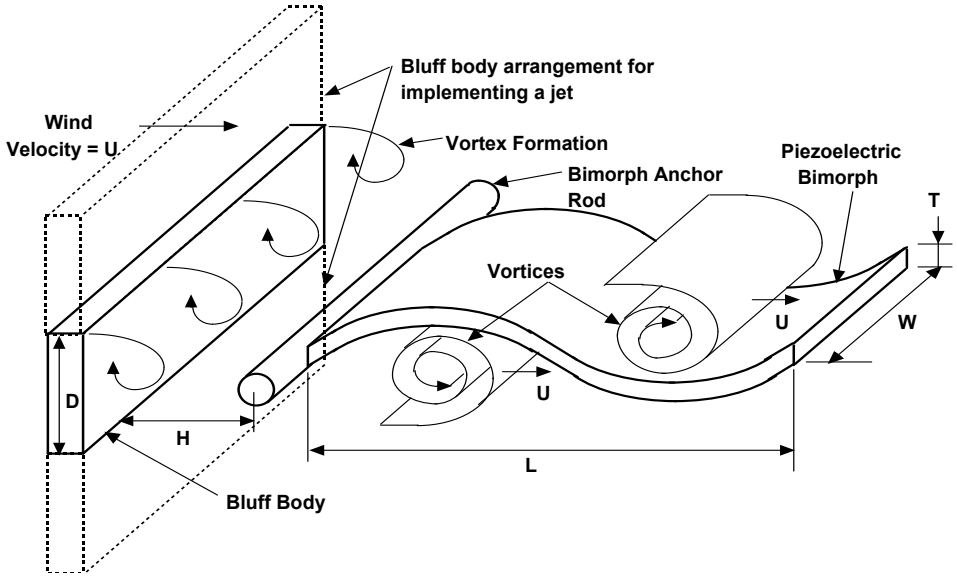

Figure 4.3. *Diagram of a bluff body showing generation of vortices to enhance the flapping amplitude of the piezoelement. Both a standard bluff body (solid line) and an arrangement (dotted lines) to implement the slit or jet are shown.*

The material of the bluff body was not important for testing, therefore a PVC pipe was chosen for the anchor and bluff body due its ease of attachment to the wind tunnel. A PVC pipe will ensure reliability and robustness under harsh weather conditions as well.

No experiments in this research used bluff bodies over 10cm in diameter due to the limited height of wind-tunnel openings. Further research using larger bluff bodies will be carried out to see if in fact, piezoelement and vortex shedding frequency coupling can be achieved and what advantages it proposes. Coupling between the vortex street shedding frequency and piezoelement oscillation frequency could enhance the efficiency of the overall wind-to-electric piezo energy system.

4.2 Increasing the Electrical Energy Extraction

The standard full-wave rectifier bridge gives a means to convert alternating current (AC) electrical signals to direct current (DC) signals via rectification. This is accomplished by using a diode bridge and a large storage capacitor which is shown in **Figure 4.4a**. With a conventional full-wave rectifier and a capacitive source, the optimal load resistance is expressed by Equation 4.3, where T_s is the period of bimorph oscillation, C_s is the bimorph capacitance, and $R_{Load,opt}$ is the optimum load resistance [6].

$$R_{Load,opt} = \frac{T_S}{4C_S} \qquad \text{(Equation 4.3)}$$

A PVDF unimorph (single sheet) with dimensions 10" X 8" X .002" has a source capacitance of approximately 100nF. Based on Equation 4.3, the PVDF unimorph oscillating at a frequency of 5Hz has an optimum load resistance of 500kΩ. A PVDF bimorph (two unimorphs) having a source capacitance of 200nF and a vibration frequency of 5Hz has an optimum load resistance of 250kΩ.

The optimum load resistance for a d_{31} mode MFC-PZT having a source capacitance of .35μF and an oscillation frequency of 5Hz has an optimum load resistance of approximately 150kΩ. The optimum load resistance for d_{33} mode MFC-PZT having a source capacitance of 15nF is 3.3MΩ. The maximum output power at optimum load is expressed by Equation 4.4.

$$P_{Rload,opt} = \frac{V_S^{\,2}}{4R_{Load,opt}} \qquad \text{(Equation 4.4)}$$

Initial calculations were performed to get an idea of how much power one should expect from a piezoelectric transducer utilizing a conventional full-wave rectifier. Typical output voltage values were used in estimating output power. Based on Equation 4.4, the maximum output power of a PVDF unimorph voltage source having amplitude of 50V is 1.25mW. The maximum output power of a bimorph voltage source having amplitude of 100V is 10mW. The maximum output power of a d_{33}-mode MFC-PZT with an

open-circuit voltage of 250V is 4.7mW. The maximum output power of a d_{31}-mode MFC-PZT with an open-circuit voltage of 50V is 4.2mW.

When piezoelectric devices are used as power generators, resonant systems are required to overcome the low coupling factor. Direct electrical resonance is not practical for the wind-generated electricity piezoelectrics because the low frequency of the piezoelement motion (5-10Hz) necessitates impractically large inductor values [1]. A quasi-resonant circuit which overcomes this limitation is a Series Synchronized Switch Harvesting on Inductor (SSSHI) circuit. SPICE simulations have shown that SSSHI can provide up to four times the maximum power output than that of a conventional full-wave rectifier given realistic passive components and switches.

Circuit diagrams for the conventional full-wave rectifier, Series Synchronized Switch Harvesting on Inductor circuit, and switching waveforms for the SSSHI circuit are displayed in **Figure 4.4** [5].

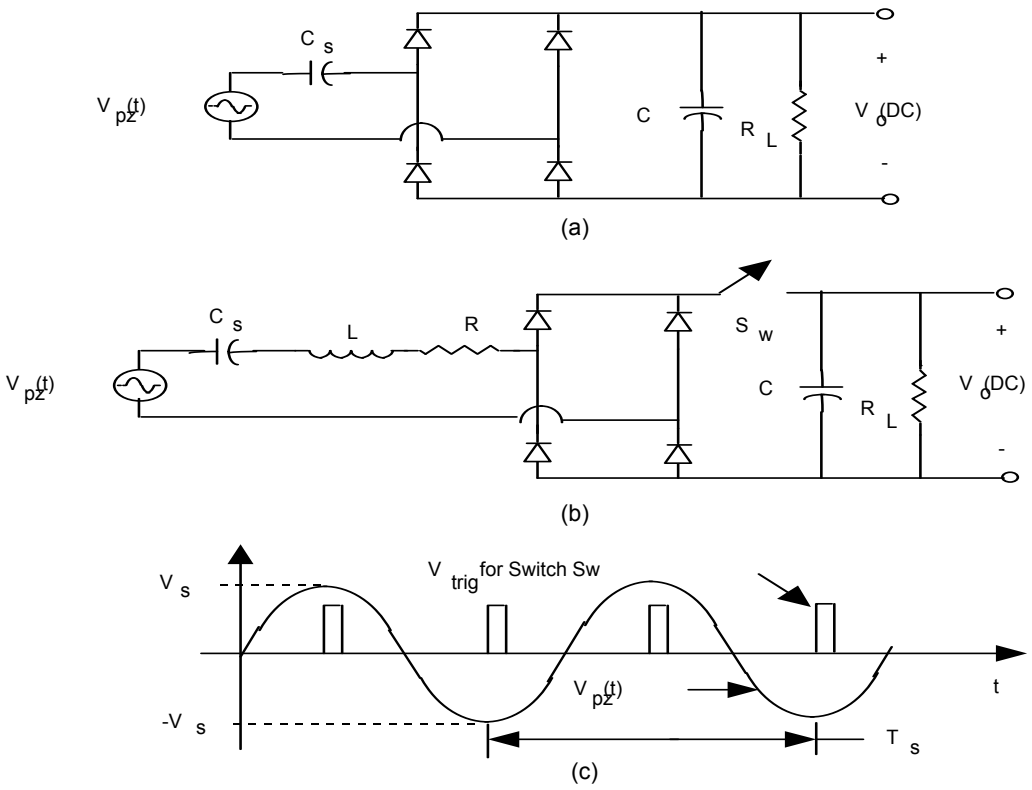

Figure 4.4 *electrical energy extractions from piezoelement using (a) standard full-wave rectifier and (b) using a synchronized switched inductor or quasi-resonant rectifier. Trigger signal timing for closing the switch is shown in (c).*

As illustrated in **Figure 4.4(b)**, the resonating inductor is placed on the source side of the diode bridge because this was experimentally found to be superior in performance than placing the inductor on the load side of the diode bridge. The resistor 'R' in **Figure 4.4b** represents the winding resistance of the inductor, the finite Q value of the piezoelectric and the 'on' resistance of the switch. The switch is closed at the peaks of the full-wave rectifier output for half the resonant period of the LC network. This results in lower source impedance and more output current as shown in **Appendix B**. Hence, greater maximum output power is attainable.

The optimum load resistance of the SSSHI circuit is given by Equation 4.5 (derived in **Appendix B**) where $\varphi = \pi/2Q_S$ and $Q_S = \omega L/R$ [5].

$$R_s = \frac{T_s}{4C_s}\left[\frac{1-e^{-\phi}}{1+e^{-\phi}}\right] \qquad \text{(Equation 4.5)}$$

As Q_S increases the optimum load resistance drops quasi-exponentially, therefore a high Q value is needed to achieve high SSSHI circuit performance. As Q_S goes to infinity the optimum load resistance goes to zero and maximum output power shoots to infinity. The Q_S value includes the combination of the piezoelectric dielectric loss and the losses in the inductor. Even if one were to build an ideal inductor, combined Q_S values would not exceed 50 due to the dielectric losses within the PVDF itself.

CHAPTER 5

Power Conditioning Electronics

The following chapter discusses the power conditioning electronics of the SSSHI circuit as well as the micro-power regulated step-down converter which is powered directly from the piezoelectric itself. The chapter begins with the SSSHI circuit design, focusing on the peak-triggering circuit, switch, and inductor. The later part of this chapter explains the start-up circuitry and steady-state operation of the piezo-powered regulated step-down converter.

5.1 SSSHI Circuit Design

The SSSHI circuit comprises of a diode bridge, peak triggering circuit, switch, and inductor. The peak triggering circuit was the most difficult aspect of the SSSHI circuit design requiring robustness, dependability, and above all extremely low power dissipation. The switch is implemented in BiMOS technology using discrete components. The inductor implemented in the SSSHI circuit was custom built to provide a large inductance value, yet sustain very low power dissipation at the LC resonant frequency. A diagram of the complete SSSHI circuit (excluding regulator) is displayed in **Figure 5.1**. A photograph of the complete circuit is shown in **Figure 5.2.**

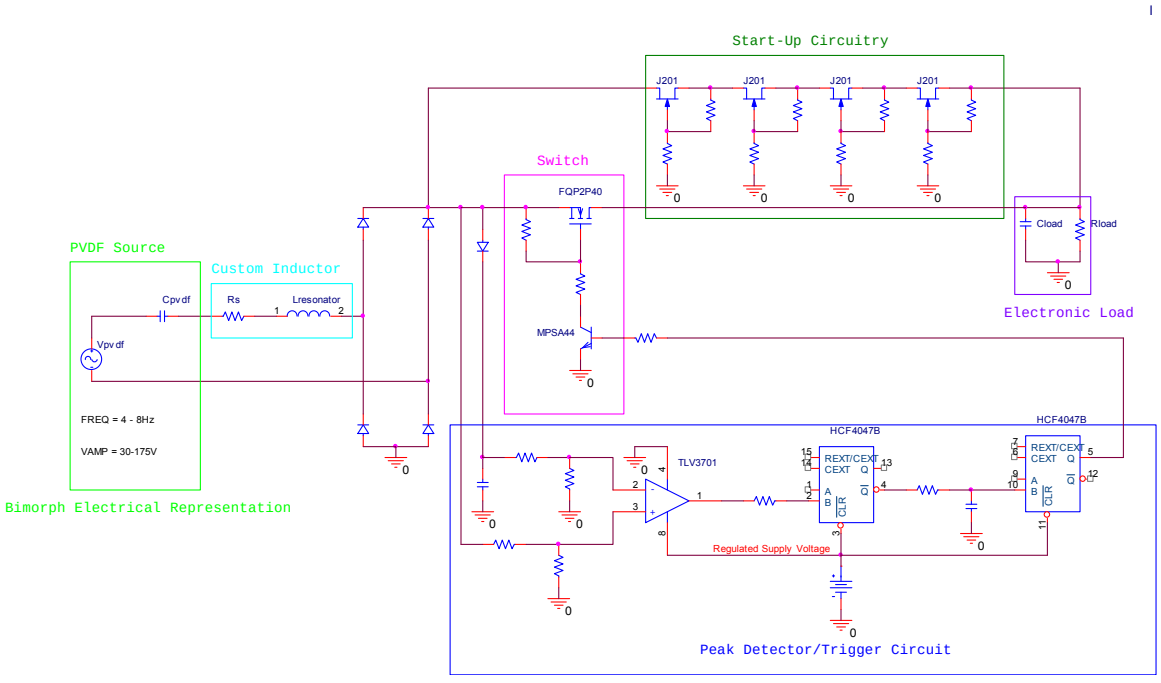

Figure 5.1 *Schematic of PVDF electrical model, full bride rectifier, peak trigger circuit, start-up circuitry, and load.*

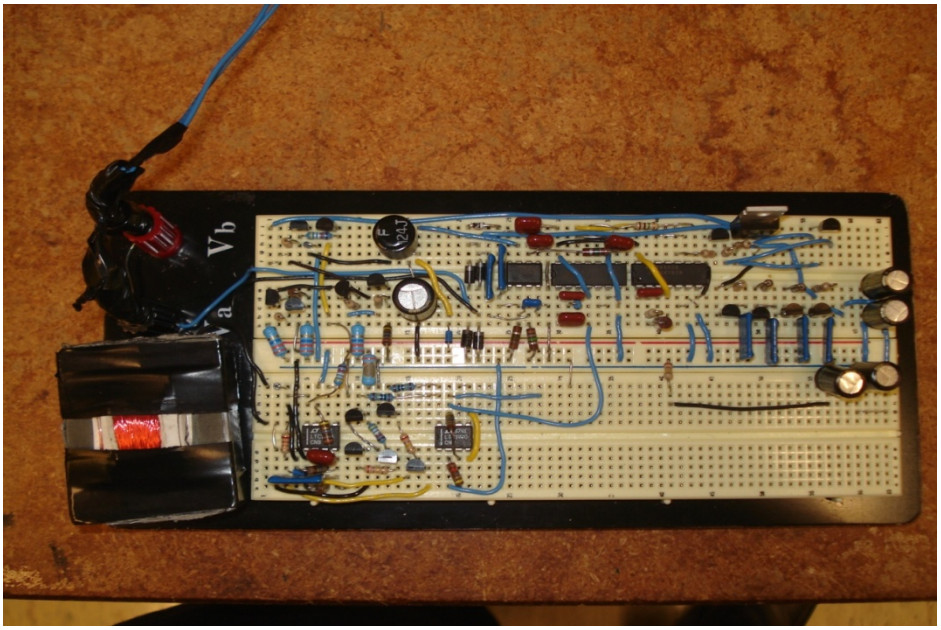

Figure 5.2 *Photograph of complete SSSHI circuit (including step-down converter). Electrical leads coming from piezoelement are shown on top left. Inductor is on bottom left corner.*

5.1.1 Peak-Triggering Circuit Design

The peak-trigger circuit contains a full-bridge rectifier, two voltage divider networks, peak detector, comparator, and two multi-vibrator ICs. The schematic of the peak-triggering circuit is shown in **Figure 5.3**.

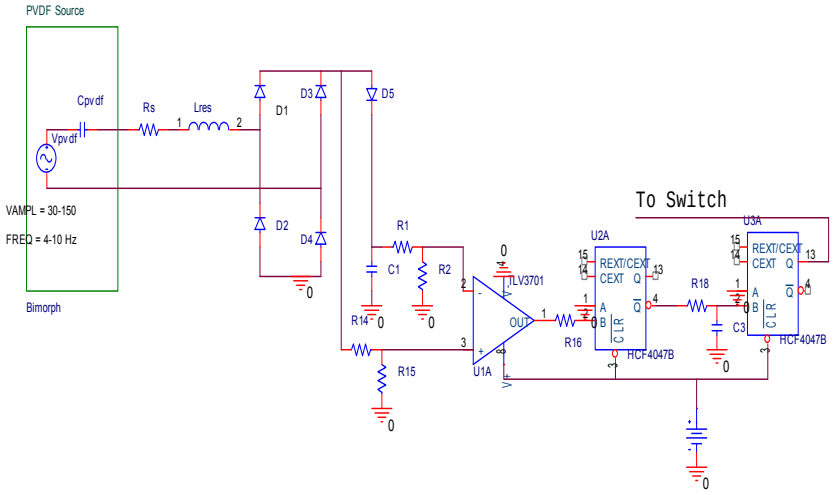

Figure 5.3 *Schematic of peak-triggering circuit used in SSSHI circuit.*

Voltage divider (R14 and R15) is used to reduce the input voltage from several hundred volts down to fewer than 3V (which is the positive power supply rail). The peak-detector (D5 and C1) and voltage divider (R1 and R2) is used to achieve a DC signal to compare to the attenuated full-wave rectifier signal. The attenuated peak-detector signal output is connected to the input of the comparator TLV3701's negative terminal. The attenuated full-wave rectifier signal is connected to the positive terminal of comparator TLV3701. The output of comparator TLV3701 goes high slightly before (10-15ms) the maximum and minimum peaks of the piezoelectric sinusoidal output voltage. This is shown in **Figure 5.4**. The slight triggering error will be compensated for by the use of an extra low power multi-vibrator or one-shot in the peak-triggering circuit.

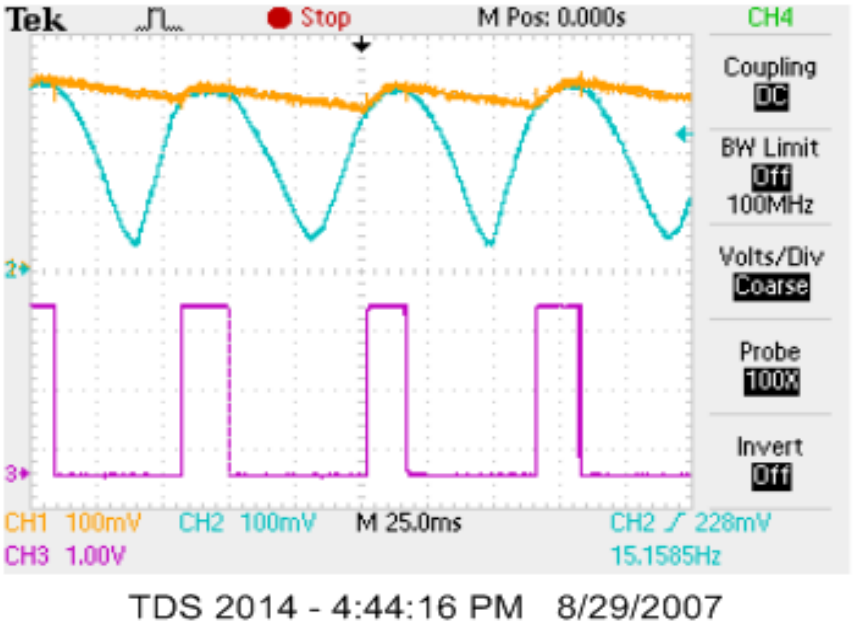

Figure 5.4 *Waveforms of comparator TLV3701. Attenuated peak-detector signal is shown on top (negative input). Attenuated FWR signal is shown in the middle (positive input). Comparator output is shown on bottom.*

After comparator TLV3701 (U1) goes high, one-shot #1's (U2-HCF4047B from ST Microelectronics) negated output goes low for a set period of time t_{delay}, which is on the order of 5-10ms depending on the resistor and capacitor values of the one-shot's RC network. The monostable output pulse is given by 2.48RC. The power dissipation of the monostable is directly proportional to the capacitance used in the RC network; therefore it is set to 6.8nF (close to the minimal suggested value given by ST which is 1nF). In

order to achieve a delay time on the order of 5-10ms the resistance value of the RC network is approximately 500kΩ (close to the maximum suggested value stated by ST Micro, which is 1MΩ).

After this set period of time one-shot #1's (U2A) negated output will go high. The output of one-shot #1 goes through a low-pass filter (to reduce noise) with a very low time constant and into the input of one-shot #2 (u3). This in turn will cause one-shot #2 (U3A) to go high for set period of time T_{ON} which is derived later on. Finally, one-shot #2 goes high, injecting current into the base of NPN BJT 'Q2', turning it on, and initiating the switching process. These waveforms are shown in **Figure 5.5**.

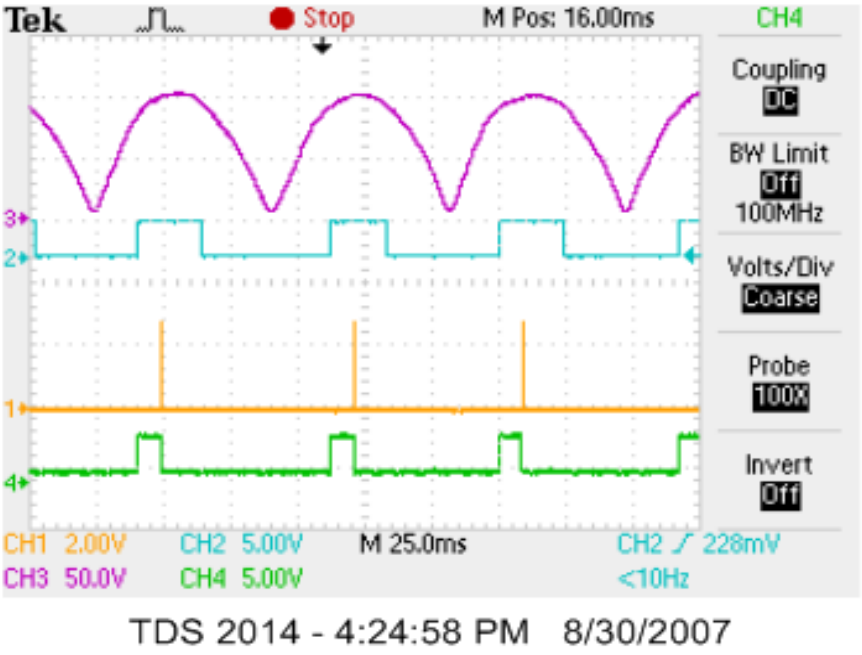

Figure 5.5 *Trigger circuit waveforms. Full-wave rectifier voltage (top). Comparator output voltage (2nd from top). One-shot#1 outputs T_{delay} when the comparator goes high (bottom). One-shot#2 output to switch (2nd from bottom).*

The reason for the first one-shot is to add some delay to the trigger signal, which is set high before the maximum and minimum voltage peaks of the piezoelectric transducer. If one switches the input terminals of the comparator, the circuit will trigger after the peaks by at least 5ms due to the comparator offset and sensitivity. This delay gives inefficiencies which are too high and renders this triggering scheme inadequate for the SSSHI circuit. By triggering 5-10ms before the maximum and minimum voltage peaks and adding some delay before actually switching, one can achieve the best AC to DC electrical conversion efficiencies with the SSSHI circuit.

Furthermore, this topology was chosen over a triggering after the peak scheme due to the inevitable delay of the triggering circuit and turn-on time of the switch which pushes the actual switching time 6-7ms past the maximum and minimum peaks. This switching inaccuracy gives rise to approximately 20% power loss compared to an SSSHI circuit triggering within 1ms of the maximum and negative voltage peaks. Thus, a triggering scheme that switches prior to the maximum and minimum peaks is implemented in the SSSHI circuit.

The ultra-low power peak trigger circuit was designed to have a negligible effect on the SSSHI circuit output voltage much like that of using an external power supply or battery. The power consumption of the peak-triggering circuit is approximately 10μA @ 3V, dissipating 30μW from the 3V supply. The power distribution of the trigger circuit is as follows:

- TLV3701 ~ 4μW
- HCF4047B_1 ~ 18μW
- HCF4047B_2 ~ 8μW

These are all the devices powered from the 3V regulated supply line. The power loss due to the diodes is expressed in Equation 5.1.

$$P_{diodes} = 4 * V_F I * D * \frac{2}{\pi} = 4(.5V)(70mA)\frac{1\%}{2} * \frac{2}{\pi} = 446\mu W \qquad \text{(Equation 5.1)}$$

The losses due to reverse leakage current are trivial. The approximate power loss due to the voltage attenuators (dividers) is expressed in Equation 5.2.

$$P_{volt\_div} = 2\left(\frac{V^2}{R_1} + \frac{V^2}{R_2}\right) = 2\left(\frac{150^2}{200M\Omega} + \frac{1.5^2}{2M\Omega}\right) = 227\mu W \qquad \text{(Equation 5.2)}$$

All other power losses of the peak-triggering circuit are considered trivial.

5.1.2 Switch Implementation

Design requirements for the switch are high off-resistance, low on-state resistance, low gate-drive, breakdown voltages on the order of 400V, and switching times on the order of 20μs or lower. The gate drive is powered from the piezoelectric itself, thus the gate drive must require little power, yet still achieve

fast enough switching not to degrade the Q value of the resonating inductor and piezoelectric capacitance. In order to achieve these switching requirements, the SSSHI switch is implemented using BiMOS technology, more specifically a NPN BJT and a P-type MOSFET. A schematic of the BiMOS switch is displayed in **Figure 5.6**.

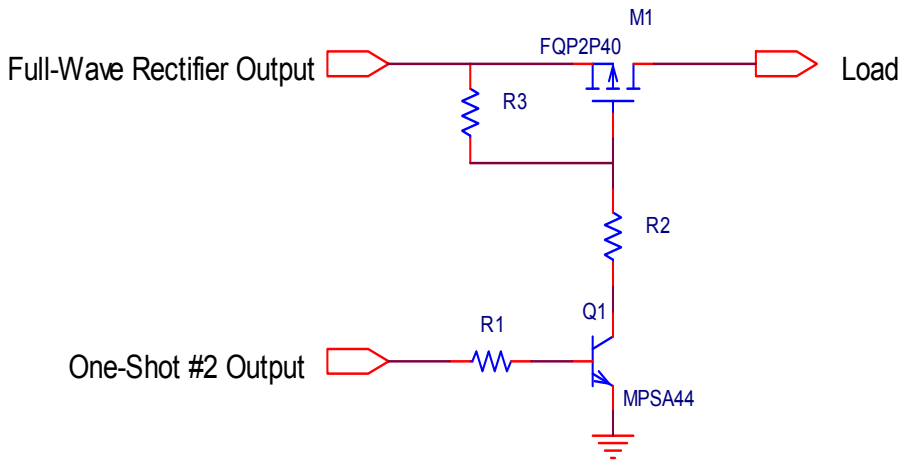

Figure 5.6 *Schematic of BiMOS switch implementation in SSSHI circuit.*

As the output of one-shot #2 (U3A) goes high, current is injected into the base of Q1 (MPSA44) turning on the transistor. This in turn drives R2 to ground. There is a voltage drop across the source-gate of M1 (FWP2P40) which is determined by the voltage divider network R2 and R3 (**Figure 5.4**). This voltage drop gives a negative gate-source voltage turning on P-channel MOSFET M1 and allowing current to flow from the full-wave rectifier output to the load.

The specific transistors chosen to implement the switch are PMOS-FQP2P40 and NPN-AMPS44. Switching times for the PMOS device are on the order of 20µs due to a gate capacitance of 200pF and a gate-source resistance (R3) on the order of 100kΩ. The switching time of the BJT is much faster than the MOSFET due to the high injecting device current (R1 < R3) and low junction capacitance of the BJT. The amount of turn-on delay of both transistors only increases the accuracy of the peak-trigger circuit since it triggers milliseconds before the maximum and minimum voltage peaks. However, the turn-off delay time of the switches dampens the performance of the SSSHI operation. This is due to the fact that the current traveling through the inductor begins to reverse when the switch is held open longer than half the period of resonance.

The on-state resistance of the PMOS device is approximately 6 ohms, which contributes very little to the degradation of the overall Q value of the SSSHI circuit. The voltage drop across the switch is approximately 260mV (46mA * 6Ω), which degrades the Q value; however, this is unavoidable with power devices. The power losses due to the on-state resistance of the PMOS switch is expressed in Equation 5.3, where V is the voltage across the PMOS when on, R is the on-state resistance, and D is the duty ratio.

$$P_{on} = \frac{V^2}{R} D = \frac{V^2}{R}\left(\frac{T_{ON}}{T_{OFF}}\right) = \left(\frac{.26^2}{6}\right) * \left(\frac{1ms}{100ms}\right) = 113\mu W \qquad \text{(Equation 5.3)}$$

The gate charge of the PMOS device is 10nC. The switching frequency is approximately 10Hz and the voltage across the gate is 10-20V depending on the voltage across the storage capacitor. The power loss due to gate charge as expressed by Equation 5.4 is trivial.

$$P_{gate} = \frac{Q_g V f}{2} = \frac{10nC(10)10}{2} = \frac{10^{-6}}{2} = .5\mu W \qquad \text{(Equation 5.4)}$$

This power is dissipated in R3 as heat. Power is also dissipated in R2 which is expressed in Equation 5.5, where V is the voltage across R2, R is the resistance value of R2, and D is the duty ratio (voltage across resistor is assumed to be roughly 5V and T_{ON} is expressed in section 5.1.3.

$$P_{R2} = \frac{V^2}{R} D = \frac{(50V)^2}{270k\Omega} * 1\% = 10\mu W \qquad \text{(Equation 5.5)}$$

The power losses due to R1 and the NPN transistor are trivial compared to the power losses in R2 and the PFET.

5.1.3 Inductor Design

The design requirements for the inductor are low power dissipation and high inductance. Low power dissipation is necessary to achieve a high Q value and furthermore an efficient energy harvesting circuit. A large inductance value is desired for longer switch on time (Equation 5.9). A longer switch on time allows the switching transients to be more forgiving (longer t_{rise}, t_{fall}, and t_{delay} times). Therefore, a ferrite core was chosen for the inductor design. Ferrites have high permeability which leads to a physically smaller inductor as well. The inductor must be able to support voltages as high as 150V base to peak. The inductor must sustain a maximum current given by the peak voltage divided by the characteristic impedance. This

maximum current (considering bimorph PVDF) is expressed in Equation 5.6, where Z_o is the characteristic impedance of the LC network.

$$I_{peak} = \frac{V_{peak}}{Z_0} = \frac{V_{peak}}{\sqrt{L_r / C_r}} = \frac{150V}{\sqrt{.92H / 200nF}} \approx 70mA \qquad \text{(Equation 5.6)}$$

In the construction of the inductor, AWG32 copper wire was wound around the ferrite core to achieve an inductance on the order of 1H. The actual inductance value was found to be .92H which is satisfactory for the SSSHI circuit design (the final one-shot on-time must be adjusted to half the resonant period of the LC network).

The switch is to be closed for half the period of the resonance between the capacitance of the PVDF and the inductor which is derived by Equations 5.7-5.9.

$$f_s = \frac{1}{2\pi\sqrt{L_r C_r}} \qquad \text{(Equation 5.7)}$$

$$T_s = \frac{1}{f_s} = 2\pi\sqrt{L_r C_r} \qquad \text{(Equation 5.8)}$$

$$T_{on} = \frac{T_s}{2} = \pi\sqrt{L_r C_r} \qquad \text{(Equation 5.9)}$$

The transistors used for the switch design have large breakdown voltages and hence larger depletion regions to withstand these voltages. When turning these devices on and off the charge must be pulled out of the depletion region. Because more charge must be pulled out of the device the switching time is increased. These high voltage devices are not going to provide fast, accurate switching for the SSSHI circuit, but if the on time of the switch is much greater than the time to turn the switch on and off, the power losses due to the slow switching will be minimized. The higher the resonating inductance of the closed switch LC network, the greater the on-time of the switch (Eq. 5.9), and hence the more forgiving the switching characteristics of the PMOS and NPN transistors are allowed to be. This was the motivation to use an inductance value on the order of 1H. With L_r = 1H and C_{pvdf} = 20nF, T_{on} is on the order of 1ms which is much longer than the switching times ($t_{on} \sim t_{off} < 50\mu s$) of the PMOS and NPN transistors used.

A relatively high saturation flux density is necessary to support 150V without core saturation, given a small cross-sectional area ferrite core. Core material 78 from Fair-Rite Corp. was chosen as the ferrite core. Having a relative permeability of 2500 and a saturation flux density of 480mT, 78 Material™ was more than sufficient to meet the inductor design requirements. Fair-Rite's 75 Material™ was also explored due to its high permeability of 5000 and saturation flux density of 400mT. A photograph of the inductor designed with 78 Material™ core is shown in **Figure 5.7**.

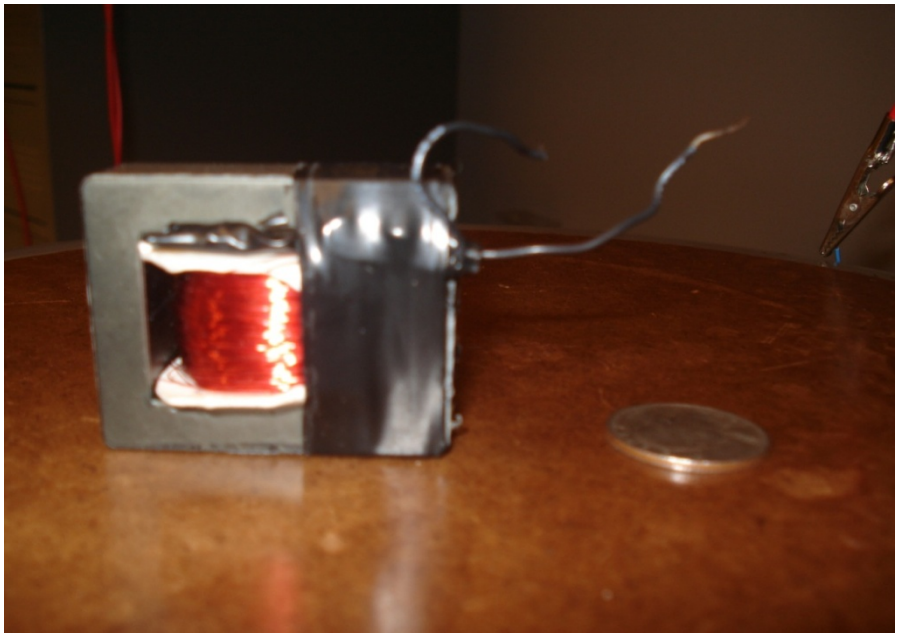

Figure 5.7 *Photograph of .92H inductor designed for low-power, high voltage energy harvesting circuit. Inductor has a Q value of 30, making it very efficient for the SSSHI circuit. A quarter is shown to give a sense of the inductor physical size.*

The inductor design specifications are expressed in Equations 5.10 – 5.11, where V_{sat} is the saturation voltage of the core, ω_0 is the frequency multiplied by 2π, B_{sat} is the saturation flux density of the core, and A_c is the cross-sectional core area.

$$V_{sat} = \omega_0 N B_{sat} A_c \qquad \text{(Equation 5.10)}$$

Given $\omega_0 = 800\pi$ rad/s, N = 600 turns, $A_c = 2.37\text{cm}^2$, and $B_{sat} = 480\text{mT}$, Vsat is calculated in Equation 5.6.

$$V_{sat} = (400Hz)(2\pi)(600turns)(.48T)(.000237m^2) = 172V \qquad \text{(Equation 5.11)}$$

A core saturation voltage of 172V is sufficient to withstand the MFC-PZT voltages as well as PVDF voltages. The saturation voltage was found to be approximately 180V experimentally. The measured inductance was found to be .92H. The series resistance is 10Ω. The Q value of the inductor was found to be approximately 30 at the resonant frequency of the PVDF capacitance, inductance resonance. The resonant frequency is expressed in Equation 5.12.

$$f_o = \frac{\omega_o}{2\pi} = \frac{1}{2\pi}\left(\frac{1}{\sqrt{LC_{pvdf}}}\right) = \frac{1}{2\pi}\left(\frac{1}{\sqrt{(.92H)(200nF)}}\right) = 371Hz \qquad \text{(Equation 5.12)}$$

An inductor was also designed using Fair-Rite 75 Material™. This ferrite core has a relative permeability of 5000 and thus allows a physically smaller inductor size to reach an inductance on the order of 1H. A photograph of the inductor is shown in **Figure 5.8**.

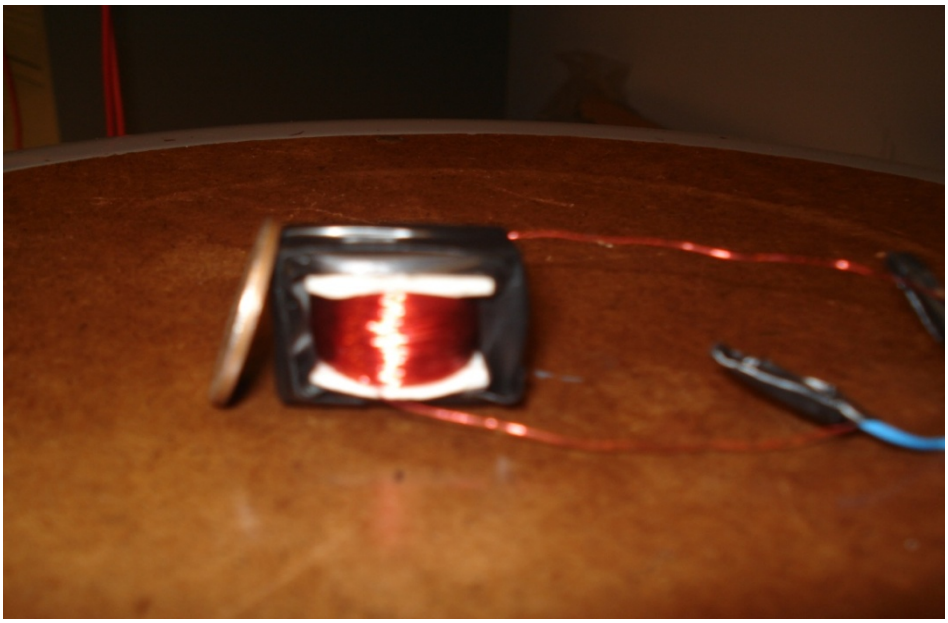

Figure 5.8 *Photograph of inductor designed using 75 Material™ from Fair-Rite. The measured inductance is 750mH. This inductor is approximately one-fourth the volume and mass of the previous inductor. Again, a quarter is shown to give a sense of inductor physical size.*

The inductor was wound using AWG32 copper wire. The measured series resistance was found to be 15Ω. The calculated Q value is approximately 30 at 400Hz. This core is very efficient when subjected to voltages less than 90V (V_{sat}), which is sufficient for MFC-PZT (d_{31}-mode) piezoelements. However, the

core saturates when using MFC-PZT (d_{33}-mode) or PVDF. The saturation voltage is expressed by Equation 5.13, which matches very close to experimental results.

$$V_{sat} = (400Hz)(2\pi)(600turns)(.40T)(.000137m^2) = 83V \qquad \text{(Equation 5.13)}$$

Both inductors designed for the SSSHI circuit have on-state losses proportional to their individual resistances. The DC resistance (DCR) of these inductors is on the order of 15-20Ω. The power losses due to the DCR are, however trivial. Because the inductor and PVDF internal capacitance is resonating @ approximately 400Hz (Equation 5.10), the AC resistance of the inductor must be calculated to give an accurate description of how much power is being lost in the inductor winding. The AC resistance of both inductors was found empirically to be approximately 100Ω at 1kHz. Inductor AC resistance values were calculated by first measuring the bandwidth of resonance and determining the Q value of each inductor. An approximate power loss due to the AC resistance of the inductor is expressed in Equation 5.14.

$$P_{R,ac} = \langle I^2 \rangle R_{ac} D = \left(\frac{(70mA)^2}{\pi} \right) (100\Omega) * 1\% = 1.56mW \qquad \text{(Equation 5.14)}$$

The inductor's winding resistance is the **critical path** of the SSSHI circuit design (besides that of the dielectric loss of the piezoelectric material). Meaning, it is the largest contributor to power loss of all the components within the SSSHI circuit. A great deal of work was put into the design of the inductor for this very reason. The hysteresis and core losses of the inductor are trivial compared to the winding losses because a ferrite core is implemented in the inductor design and switching frequency is very low (~1kHz).

5.2 Micro-power Regulated Step-Down Converter Design

The most pertinent qualities of the micro-power regulated step-down converter are extremely low power dissipation and wide-input voltage range. The peak triggering circuit requires a stable, low ripple DC power source. It is highly desirable that the regulator input power comes directly from the ambient rather than a battery. Hence, a piezo-powered, micro-power regulated step-down converter was investigated for this functionality.

The lowest power, high input voltage commercially available voltage regulator on the market is the LT1934 from Linear Technologies, which draws 12μA quiescent current and has a limited input voltage range of 4-34V. At wind speeds of 14mph and above, the MFC-PZT (d33-mode) and PVDF will output a minimum of 50Vdc across a matched load. Because the maximum input voltage of the LT1934 is 34V, one

would have to put two regulators in series or have a pre-regulator in order to drop the voltage below 34V prior to the input to the LT1934 voltage regulator. This gives rise to more power losses and added circuitry. Both of which are very undesirable in an energy harvesting circuit.

Given a quiescent current of 12μA and input voltage of 50Vdc, the minimum power dissipation in the LT1934 is 600μW with no load. The LT1934's power dissipation is far too high to use in an energy harvesting circuit with the available output power, especially if the circuitry requires two regulators. Thus, a high-input voltage range, low-power dissipation, piezo-powered voltage regulator was designed and implemented along with the SSSHI circuit.

The PVDF/PZT bimorph has an open-circuit output voltage ranging from 30-180V giving a voltage output of 15-90V across a matched load. Thus, the micro-power regulated step-down converter must have an input voltage range of at least 15-90V. The converter was designed using electrical components with extremely low power consumption. Switching frequency was minimized to reduce dynamic power losses.
The trigger circuit [**Figure 5.3**] contains a comparator and two multi-vibrators (one-shots) which have a DC bias voltage range of 2.5–11V. Thus, the step-down converter must have a regulated output voltage greater than 2.5V and less than 11V. The higher the supply voltage, the higher the power dissipation in the comparator and one-shots, therefore it is advantageous to use as small as supply voltage as possible (with some tolerance) for which the circuit still operates correctly and reliably.

The step down converter was designed to have an input voltage range of 4V to over 100V and a regulated output voltage of 3.0Vdc (±3 %). A supply voltage of 3Vdc will ensure the trigger circuit will operate correctly and power dissipation of the peak-triggering circuitry is minimized. The schematic of the micro-power regulated step-down DC-DC converter is displayed in **Figure 5.9**.

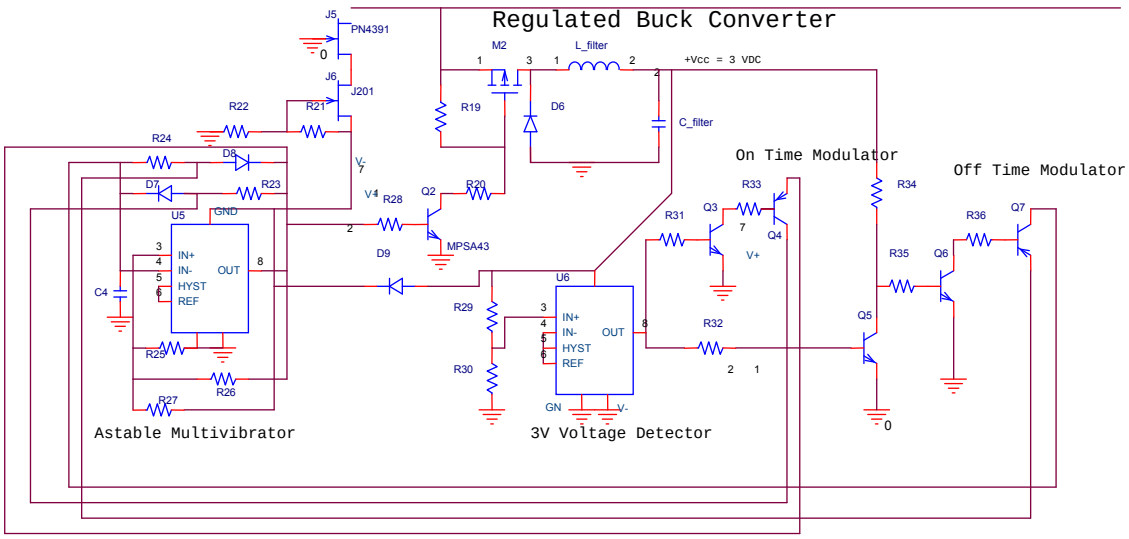

Figure 5.9 *Schematic of micro power regulated step-down converter. V_{in} comes from the top right trace (full-wave rectifier output). Input voltage has a wide range of 4 – 115V, while output remains within ±3 % of 3Vdc with SSHI switching circuit as load (10µA).*

When the piezoelement first begins to oscillate, there is no 3Vdc bias available. Special start-up circuitry as shown in **Figure 5.1** and **Figure 5.9** is required. In **Figure 5.1** JFETs J1, J2, J3, and J4 are conducting at start-up. This permits the storage capacitor to chare up via conventional full-wave rectification. The storage capacitor charges to approximately 4V, while JFETs J5 and J6 provide 2.2V to the astable comparator LTC1440 (U5) input supply. This in turn charges up C4 and astable operation begins, giving a duty cycle set by R24 and R25 which is approximately 1%. Since the frequency of astable operation is on the order of 1-10Hz (V_{in}=50V), the filter inductor is 100mH, and the load current is 10µA; the step-down converter operates far into discontinuous conduction mode (DCM). Initial charge up time to a 3Vdc regulated supply voltage is approximately 30s. The waveforms are shown in **Figure 5.10.**

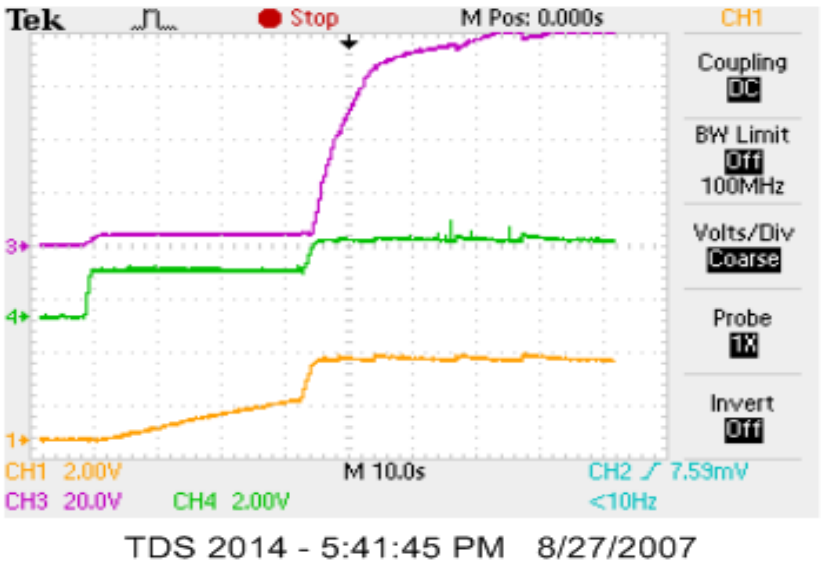

Figure 5.10 *Soft-start regulator waveforms. Storage capacitor voltage (top). Astable supply voltage (middle). Regulated output voltage (bottom).*

The 3V supply voltage gives a sufficient margin from the minimum DC supply voltage of 2.5V in addition to a schottky diode voltage drop of 300mV. Therefore, JFETs J1 and J2 will shut off completely when a 3V supply voltage is reached and astable comparator U5 will sustain its power flow from the 3V regulated supply voltage via diode D9, and not the storage capacitor. This minimizes the regulator's power dissipation because the astable supply current is drawn from 3V and not 50V through two JFETs (storage capacitor).

As the output voltage attempts to go higher than 3V, voltage detector comparator U6 goes high turning on transistor Q3 and hence Q4 and turning off Q5 and Q7. This in turn decreases the on-time of astable comparator U5. By decreasing the on-time of astable comparator U5 and hence the duty ratio, the output voltage is reduced.

As the output voltage attempts to fall below 3V, the voltage detector comparator output goes low turning off transistors Q3, Q4 and Q5, turning on transistors Q6 and Q7. This in turn decreases the off-time of astable comparator U5. By increasing the on-time of astable comparator U5 and hence the duty ratio, the output voltage is increased. The transition times of the astable switches are approximately 5µs, giving rise to a regulated output voltage within ±3% of 3V. The regulated output voltage is shown in **Figure 5.11**.

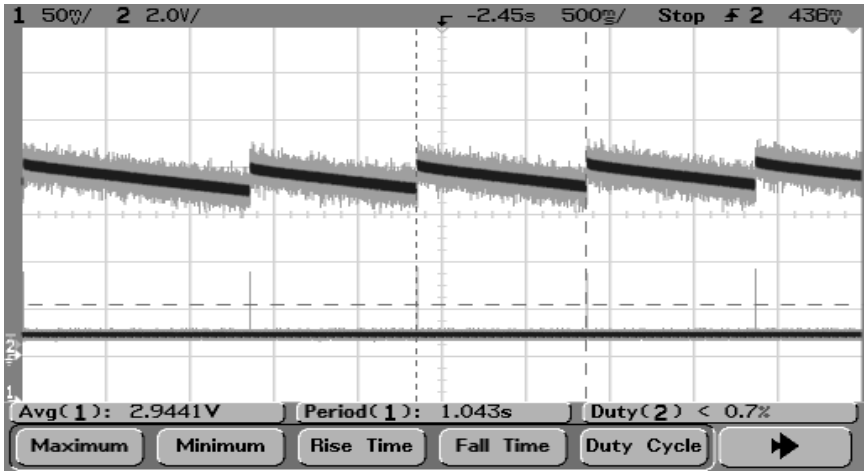

Figure 5.11 *Output voltage of micro-power regulated buck converter. Switch drive signal is shown on bottom. Duty cycle is approximately 0.2 %. Peak to peak ripple is approximately 70mV.*

Because the regulated step-down converter dissipates roughly 60µW, it is inefficient for light loads (less than 100µW) and very efficient at larger loads (greater than 1mW). The trigger circuit draws approximately 10µA at 3V. This gives rise to a very inefficient step-down converter (approximately 30 %), yet it only dissipates a meager 60µW. This is a fraction of the total power generated by the addition of the SSSHI circuitry.

A schematic of the complete circuit is shown in **Figure 5.12** and a table showing the component values is given in **Table 5.1**.

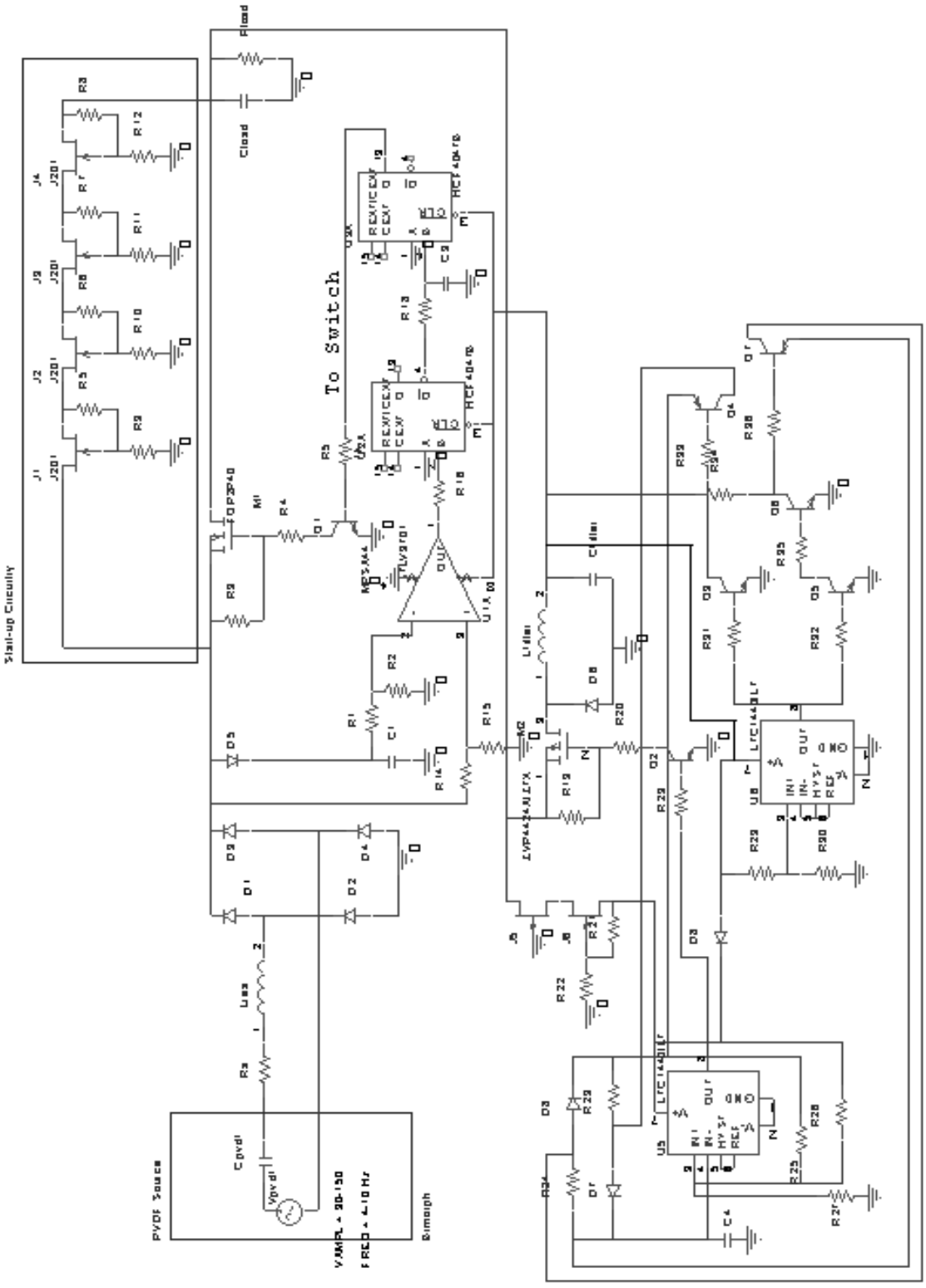

Figure 5.12 *Complete schematic of power conditioning electronics*

Component	Description	Component	Description
D1	HER104 - 400V diode	R26	18 MΩ
D2	HER104 - 400V diode	R27	18 MΩ
D3	HER104 - 400V diode	R28	270 kΩ
D4	HER104 - 400V diode	R29	18 MΩ
D5	BAT41 - 100V schottky diode	R30	12 MΩ
D6	BAT41 - 100V schottky diode	R31	1 MΩ
D7	BAT41 - 100V schottky diode	R32	1 MΩ
D8	BAT41 - 100V schottky diode	R33	270 kΩ
D9	BAT41 - 100V schottky diode	R34	33 MΩ
ESR1	Equivalent	R35	499 kΩ
R1	200 MΩ	R36	270 kΩ
R2	1.8 MΩ	R_load	Variable load resistance
R3	120 kΩ	C_pvdf	200 nF
R4	270 kΩ	C1	6.8 nF - ceramic
R5	200 MΩ	C2	6.8 nF - ceramic
R6	200 MΩ	C3	6.8 nF - ceramic
R7	200 MΩ	C4	6.8 nF - ceramic
R8	200 MΩ	C_filter	1 mF – electrolytic
R9	18 MΩ	C_load	4 - 33 µF - electrolytic
R10	18 MΩ	L_filter	100 mH, Rs = 70Ω
R11	18 MΩ	Lr	.92 H, Rs = 15Ω (custom)
R12	18 MΩ	M1	FQP2P40 - PMOS (400Vbo)
R13	270 kΩ	M2	ZVP4424A- PMOS (200Vbo)
R14	200 MΩ	Q1	MPSA44 - N-type BJT (400Vce)
R15	1.8 MΩ	Q2	MPSA43 - N-type BJT (200Vce)
R16	1 MΩ	Q3	2N3904 - N-type BJT (30Vce)
R17	1 MΩ	Q4	2N3906 - P-type BJT (30Vce)
R18	1 MΩ	Q5	2N3904 - N-type BJT (30Vce)
R19	270 kΩ	Q6	2N3904 - N-type BJT (30Vce)
R20	499 kΩ	Q7	2N3906 - P-type BJT (30Vce)
R21	12 MΩ	U1	TLV3701 - Comparator
R22	33 MΩ	U2A	HCF4047 - One-Shot Multivibrator
R23	23 kΩ	U3A	HCF4047 - One-Shot Multivibrator
R24	200 MΩ	U4	LTC1440 - Comparator w/ REF
R25	18 MΩ	U5	LTC1440 - Comparator w/ REF

Table 5.1 *Bill of Materials (BoM) for SSSHI circuit.*

CHAPTER 6

Results and Fatigue Testing

The following chapter shows the best results obtained from the piezoelements constructed in this research. It also discusses the endurance of the bimorph piezoelement and its performance after 2 million of cycles.

6.1 Results with PVDF

This thesis reports a theoretical model for determination of generated electric power from piezoelectric bimorph transducers in low frequency range far from the mechanical resonance of the piezoelement. The model is divided into two parts. In the first part, the open circuit voltage response of the transducer subjected to alternating stresses is computed based on the bending beam theory for bimorph. In the second part, this open circuit voltage acts as the input to the equivalent circuit of the capacitor connected across a purely resistive load.

The best results to date from a bimorph element using two full sheets of PVDF (10" X 5" X .002" each sheet) is 36mW across 100kΩ load employing SSSHI at an approximate wind speed of 20mph. A photograph of the full-sheet bimorph prototype is shown in **Figure 6.1**.

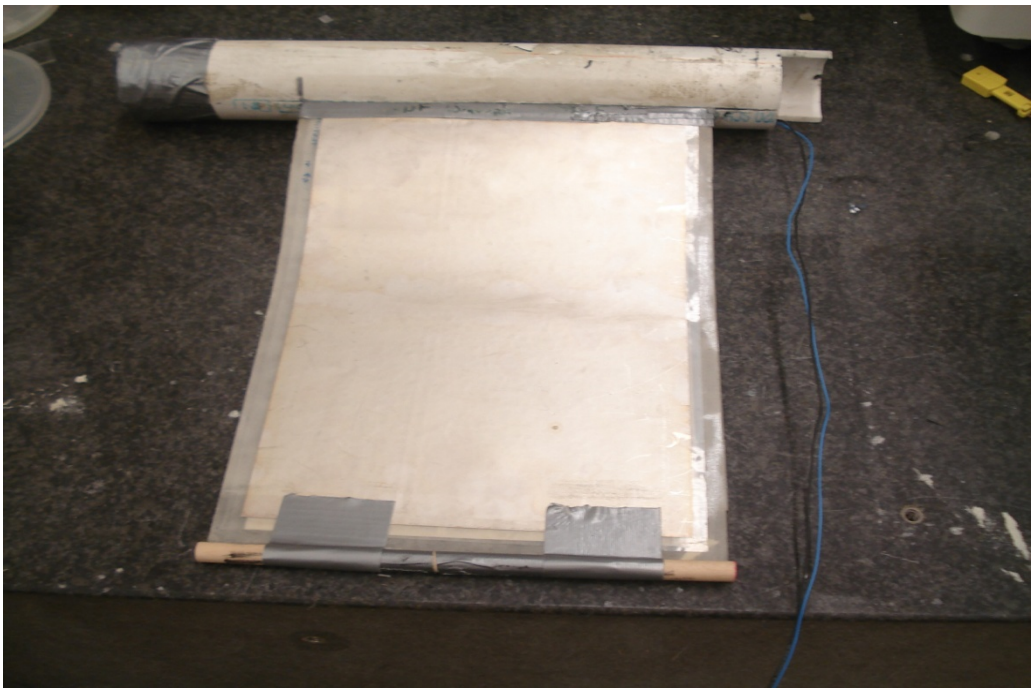

Figure 6.1 *Photograph of the full-sheet PVDF bimorph prototype.*

The best results to date from a single 10” x 8” x .002” sheet of PVDF is 36mW DC power across a 100kΩ load employing SSSHI at an approximate wind speed of 20mph (kinetic (wind) energy to DC electrical energy conversion efficiency is approximately 0.2%). This was accomplished by using two half-sheets of PVDF (5” x 8” x .002”) in a bimorph configuration. The half-sheet bimorph constructed has the actual PVDF attached closer to the free end of the flag as shown in **Figure 6.4**. Please note the peak strain is at approximately 1/2 the length of the bimorph and not at the free end with added weights. This was found empirically by placing several isolated PVDF sections along the length of the substrate and measuring the open-circuit voltage at a given wind speed. A photograph showing the multi-piezoelement prototype is displayed in **Figure 6.**2. The experimental results are shown in **Figure 6.3**.

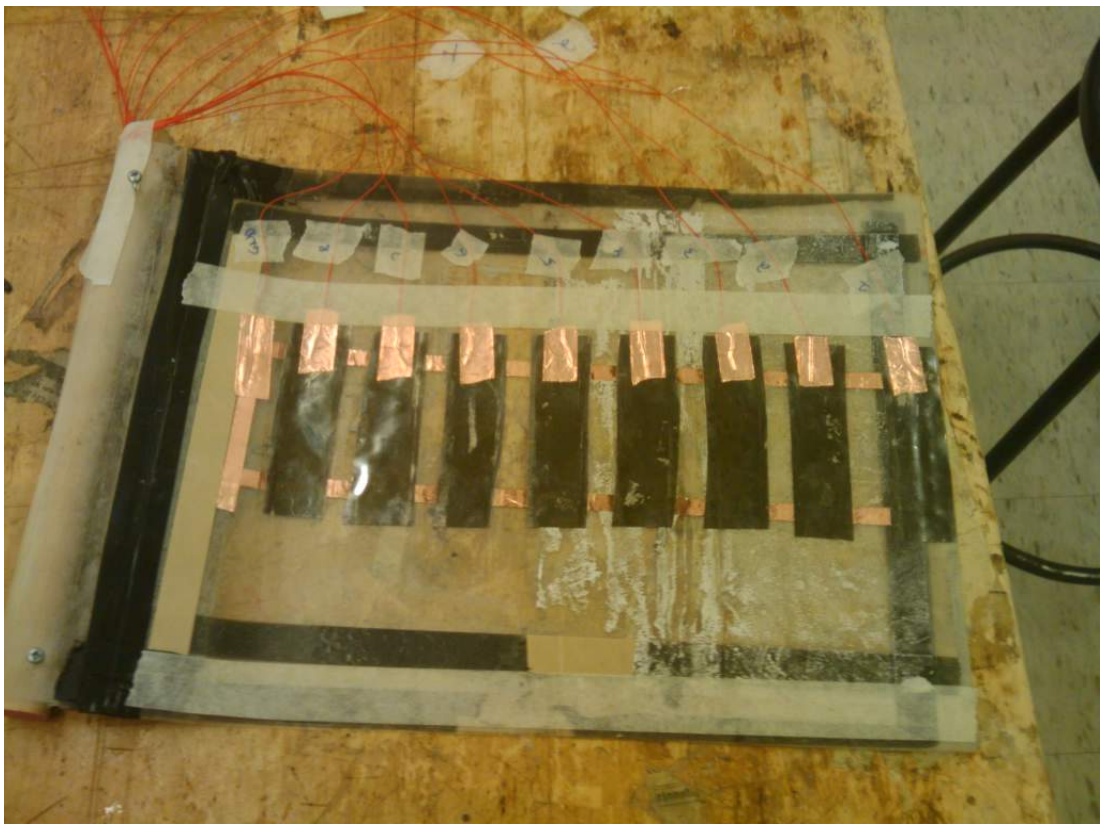

Figure 6.2 *Isolated piezoelement prototype for measuring strain levels across the length of the flag.*

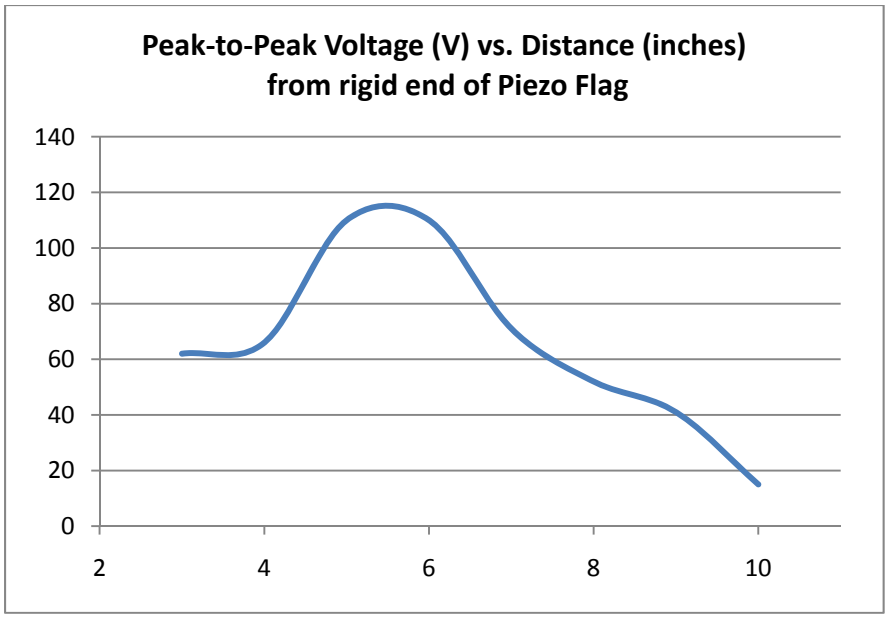

Figure 6.3 *Open-circuit voltage as a function of distance from piezoelement rigid end.*

The half sheet bimorph performed better than full-sheet bimorph due to a number of reasons: the half-sheet bimorph was constructed using 3M tape adhesive instead of spray-on adhesive which greatly increased the overall flexibility of the piezoelement, the half-sheet piezoelement had a higher oscillation frequency and higher Q value than that of the full sheet bimorph (decreasing the effective source impedance (Equation 4.5)) and most importantly, the bimorph piezoelement length is less than half the wavelength of the flag mechanical oscillation frequency. The half-sheet bimorph design incorporates strategically placed piezoelements where strain magnitude is not only large, but positive. The half-sheet bimorph therefore, has no energy cancellation throughout the piezoelement membrane.

The full-sheet bimorph covers the complete area of the flag and is subjected to positive and negative strains within any given instant of time. This energy cancellation renders the full-sheet bimorph inefficient and subsequent designs should consider the energy cancellation effect of opposite strains on the flag. A photograph of the half-sheet bimorph prototype is displayed in **Figure 6.4**.

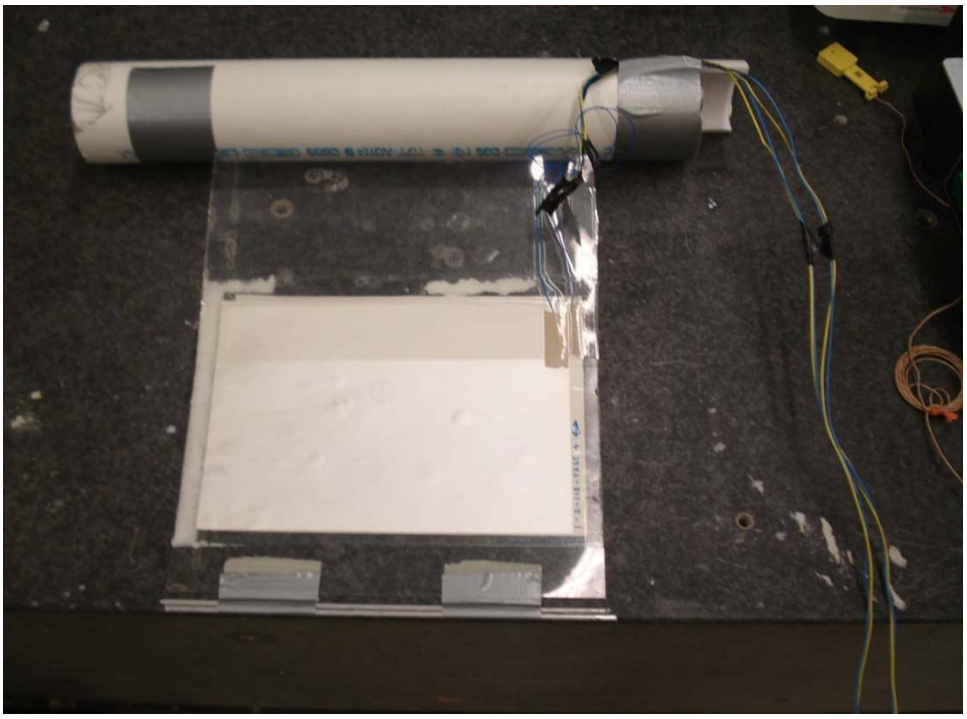

Figure 6.4 *Photograph of half-sheet PVDF bimorph prototype.*

The open-circuit voltage across the PVDF half-sheet bimorph element is shown in **Figure 6.5**.

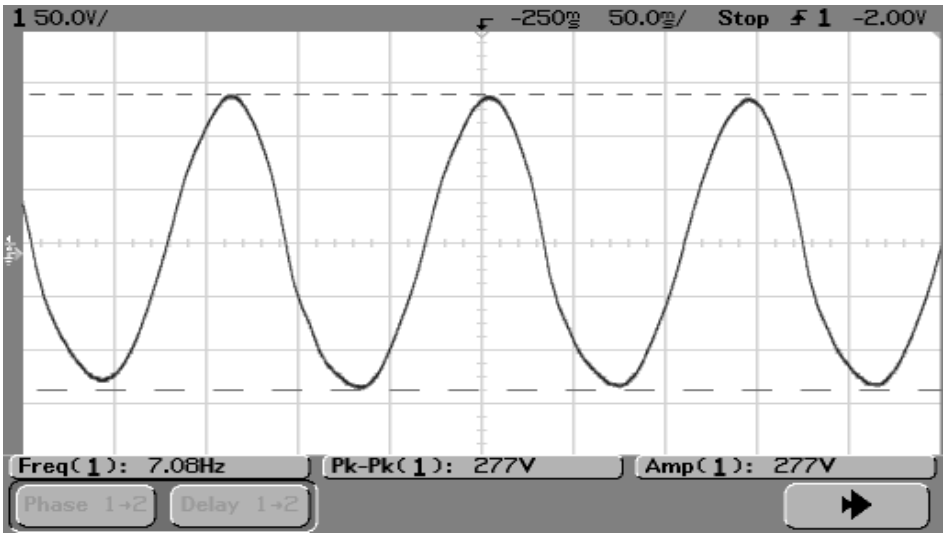

Figure 6.5 *PVDF open-circuit voltage at a wind speed of 18mph inside a small wind tunnel. The PVDF output voltage is sinusoidal with small variations in amplitude and frequency given a constant wind speed.*

The SSSHI circuit performed well with the PVDF piezoelement due to the small variations in amplitude and frequency given a constant wind speed. This gave the SSSHI triggering circuit the ability to reliably detect the maximum and minimum peaks of the PVDF output voltage. Trigger circuit waveforms of the SSSHI circuit are shown in **Figure 6.6**.

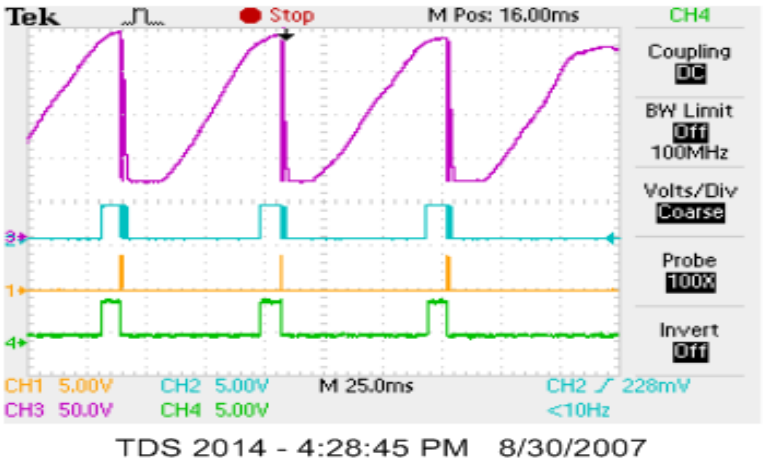

Figure 6.6 *Experimental trigger circuit waveforms. Full-wave rectifier output voltage (top). Comparator output (2nd from top). One-shot#1 output (bottom). One-Shot #2 output (2nd from bottom).*

Figure 6.7 (shown below) exemplifies the critical operation of the SSSHI circuit. The voltage seen across the piezoelement in series with a resonating inductor is reversed when the switch is closed from the rectifier bridge to the load for half the resonant period of the LC network. **Figure 6.8** shows the PSPICE simulation waveforms.

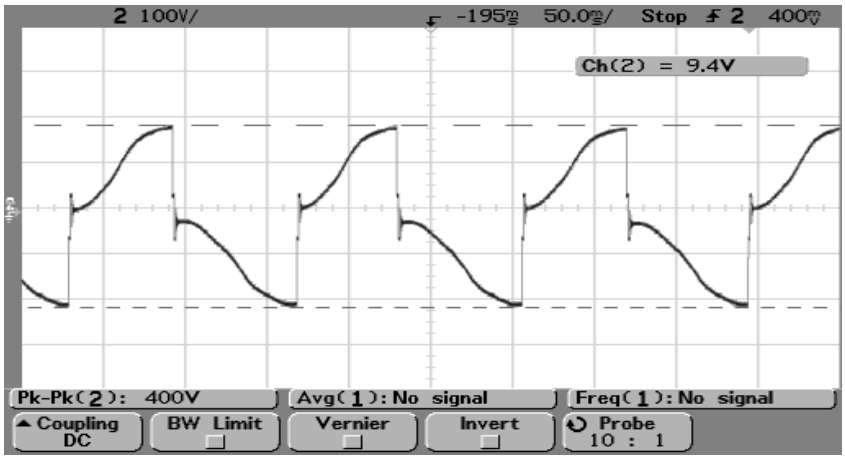

Figure 6.7 *Diode bridge input voltage. The voltage is reversed at the maximum and minimum peaks due to the SSSHI circuit.*

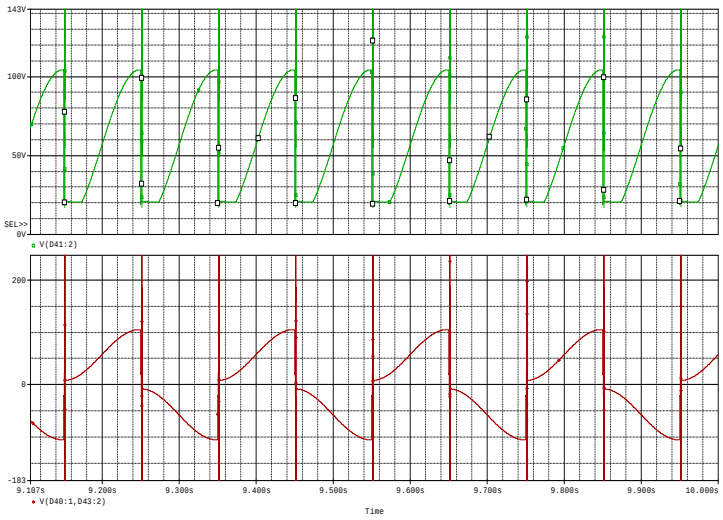

Figure 6.8 *PSPICE simulation of full-wave rectifier voltage (top) and input voltage to diode bridge (bottom).*

The peak-trigger circuit performs very well, triggering within a few milliseconds of the positive and negative peaks of the PVDF AC output voltage. The experimental waveforms match the PSPICE waveforms very closely, displaying the beautiful execution of the SSSHI circuit.

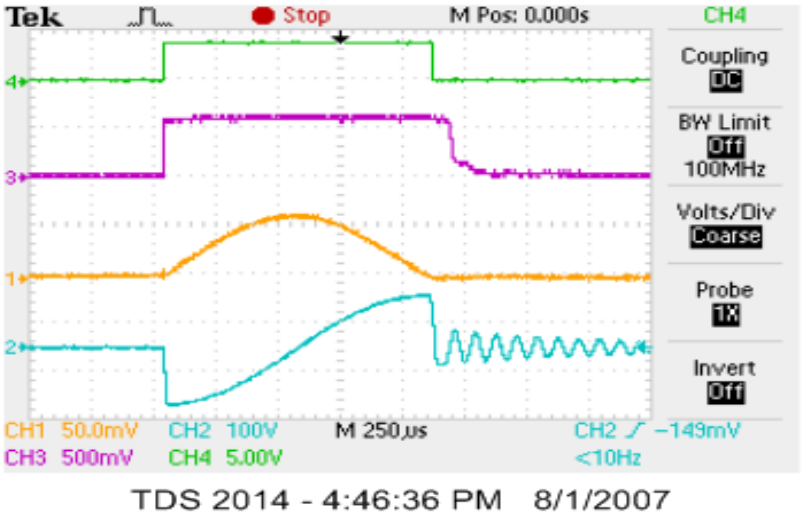

Figure 6.9 *Experimental waveforms of SSSHI circuit as the switch is closed and opened. One-Shot #3 output (top). NPN MPSA44 base-emitter voltage (second from top). Inductor current (second from bottom). Inductor voltage (bottom).*

There are some oscillations seen at the opening of the switch in **Figure 6.9**. This is due to the inductor resonating with the junction capacitance of the P-MOSFET. The power losses due to resonance at switch opening are considered trivial due to their small amplitude low duty cycle.

A plot of load resistance versus output power is shown in **Figure 6.10**. The SSSHI circuit increases the maximum output power by approximately a factor 2. This is well below the theoretical factor of four that the SSHI is supposed to give due to the very low Q value of the LC resonance. A Q value of 1.8 matches theory reasonably well to the experimental values measured.

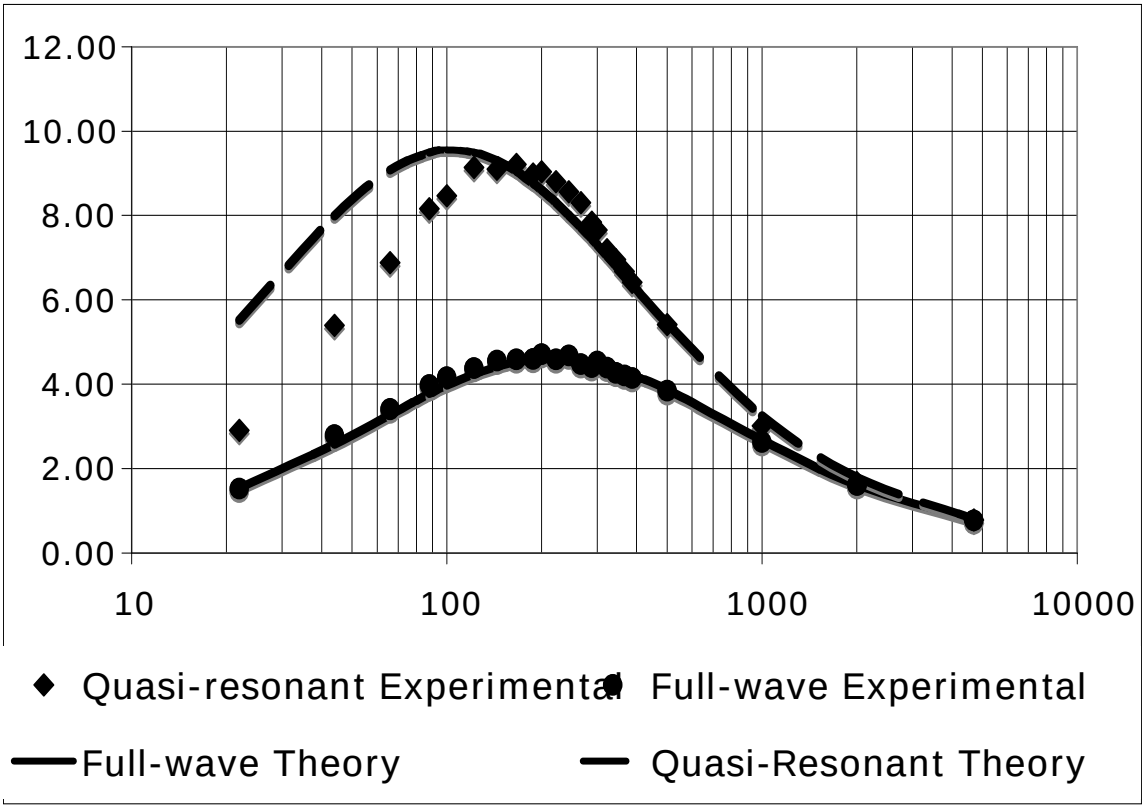

Figure 6.10 *Experimental and theoretical comparison of energy extraction from a flapping piezo element via a full-wave rectifier and a quasi-resonant rectifier at 15 mph wind speed. Output power increase by a factor of 2 with the SSSHI (Quasi-resonant) circuit versus a standard full-wave rectifier.*

By simply replacing the inductor (.47H, R_{series} = 570Ω from J.W. Miller) having a Q value of 10 with a new inductor designed specifically for energy harvesting in low power applications (Q of 30), the performance of the SSSHI circuit increases dramatically. This can be seen in **Figure 6.11** and **Figure 6.12**.

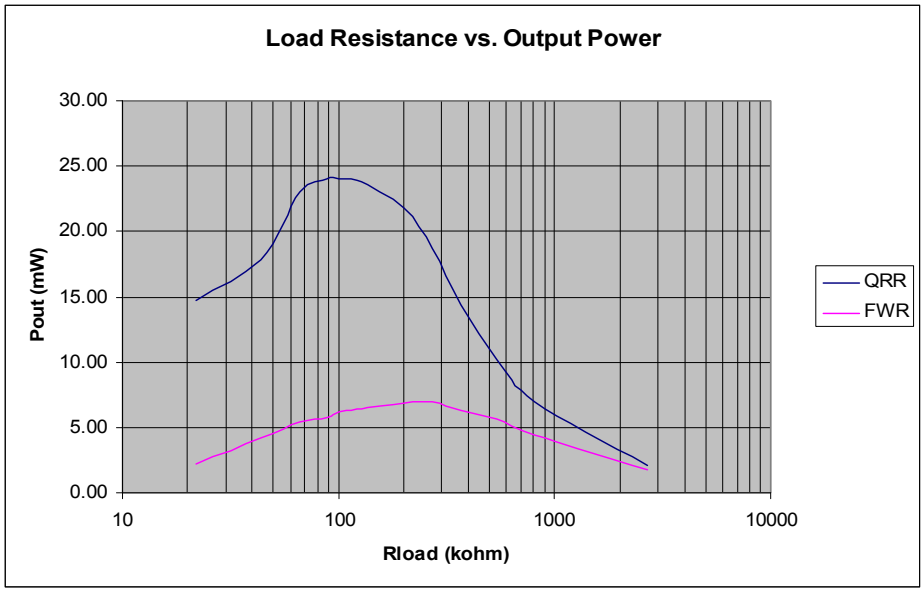

Figure 6.11 *Load resistances versus output power of SSSHI (QRR) circuit with PVDF piezoelement. Output power is graphed for conventional full-wave rectifier (FWR) as well. The SSSHI circuit gives approximately 3.5 times maximum output power than that of conventional full-wave rectifier. Measurements were taken at a wind speed of 20mph using a half-sheet bimorph piezoelement.*

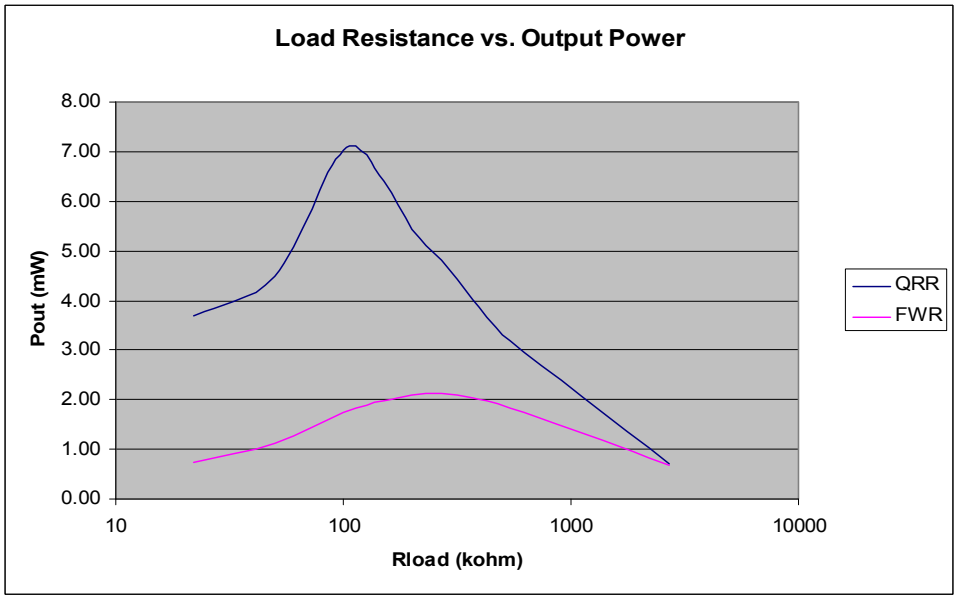

Figure 6.12 *Power output as a function of load resistance is plotted for the conventional full-wave rectifier and SSSHI circuit. Measurements were taken at a wind speed of 14mph. Open-circuit voltage is 100V.*

The empirical Q value was approximately eight in the experiments with a custom inductor. The SSSHI circuit increases the maximum output power by of a factor of 3.5 and decreases the optimum load resistance by a factor of 2.5 compared to that of a standard full-wave rectifier or direct-discharge method. This matches well with theory given a resonant Q value of 8. The optimal load impedance decreases by a factor of approximately 2.7 ($.373^{-1}$) which is expressed in Equation 6.1.

$$\frac{R_{SSHI,opt}}{R_{FWR,opt}} = \frac{\frac{T_s}{4C_s}\left[\frac{1-e^{-\phi}}{1+e^{-\phi}}\right]}{\frac{T_s}{4C_s}} = \left[\frac{1-e^{-\phi}}{1+e^{-\phi}}\right] = \tanh\left(\frac{\pi}{Q}\right) = \tanh\left(\frac{\pi}{8}\right) = .373 \qquad \text{(Equation 6.1)}$$

The inductor was also placed on the load side of the diode bridge and power measurements were taken to compare its performance against keeping the inductor near the PVDF (on the source side of the full-bridge rectifier). The results are given in **Figure 6.13**.

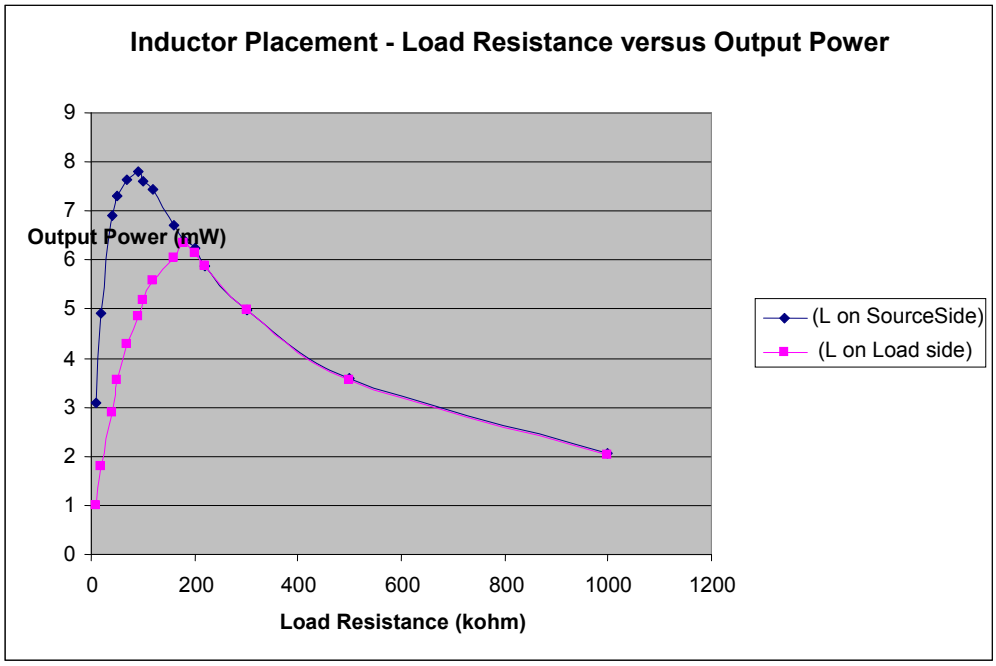

Figure 6.13 *SSSHI performance with inductor placed on source side of diode bridge and load side of diode bridge. Measurements were taken from a PVDF bimorph at a wind speed of 14mph.*

The SSSHI circuit did perform better when the inductor was connected directly in series with the piezoelectric compared to connecting the inductor on the load side of the diode bridge. Therefore, the former was used in this study.

PVDF output voltage was measured as a function of wind speed. Measurements were only taken using a conventional full wave rectifier and optimum load. This was done due to the fact that the SSSHI circuit does not perform as well at higher wind speeds due to the non-sinusoidal nature of the PVDF & MFC-PZT output voltage giving rise to unreliable, off-peak triggering. The conventional full-wave rectifier output power versus wind speed results are shown in **Figure 6.14**.

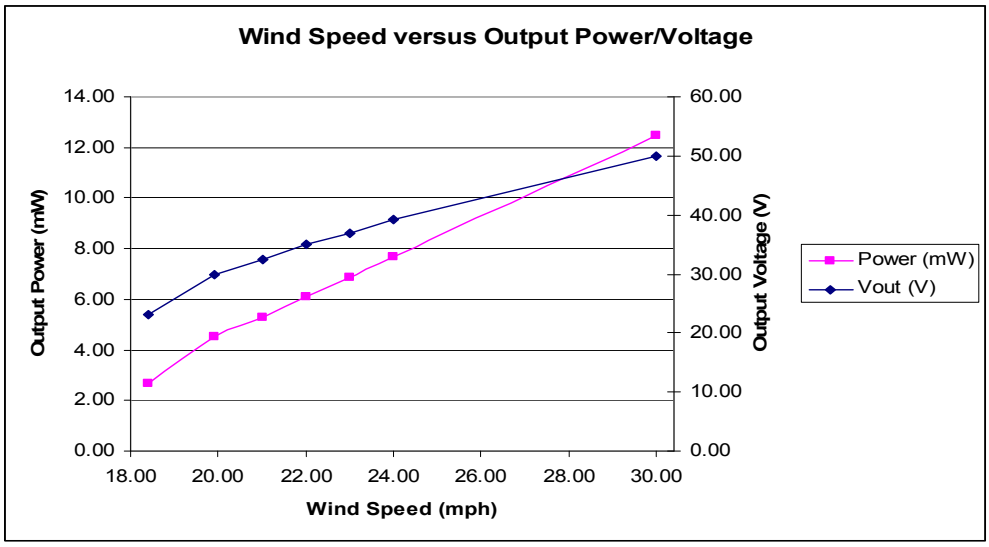

Figure 6.14 *Wind speed versus output power measurements for full-wave rectifier. Peak-to-peak voltage is also shown as a function of wind speed. Measurements were taken from a half-sheet bimorph PVDF piezoelement.*

This graph shows a linear relationship between wind speed and output power of the PVDF across an optimum load. The graph also shows a linear relationship between wind speed and output voltage. The theoretical cubic ratio between wind speed and available power is not seen in this graph. This is mostly like due to the following reasons: the higher strains of the piezo element reaching a maximum strain level of the PVDF and the tape adhesive giving way when higher strains are applied.

Frequency measurements were also taken as a function of wind speed. However, the oscillation frequency of the piezoelement did not change by more than ±5% when varying the wind speed from 18mph to 30mph.

Once the wind-speed to achieve the Kelvin-Helmholtz instability is reached, the piezoelement begins to flutter aggressively and at a steady pace. As wind speed is increased beyond the point of reaching the Kelvin-Helmholtz instability, the piezoelement begins to flap more violently. However, the frequency of oscillation is hardly a function of wind speed. This is due to the added mass on the free end of the piezoelement increasing the amplitude of oscillation with increasing wind speed, thus stabilizing the flutter frequency.

The system behaves similarly to a mass and spring. When you add more energy to the system (i.e. pull the spring further) you will see increased amplitude of oscillation, however the frequency of oscillation will remain constant (as it is only a function of the spring constant and the mass of the system). The mass added to the free end of the piezoelement acts as negative feedback to the fluttering frequency. This negative feedback explains why the frequency of oscillation of the piezoelement does not increase with increasing wind speed.

6.2 Results with MFC-PZT

The MFC-PZT output voltage is somewhat non-sinusoidal. The open-circuit voltages across the MFC-PZT (d33-mode & d31-mode) are shown in **Figure 6.15**.

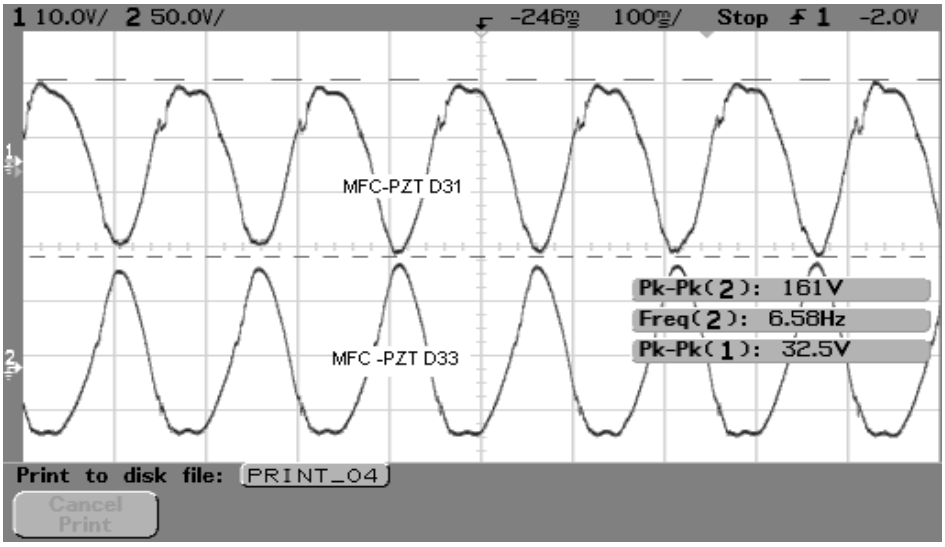

Figure 6.15 *Open-circuit voltage waveforms of MFC-PZT piezoelements.*

Due to the many 'bumps' in the sinusoidal output voltage given by the MFC-PZT, the peak-triggering circuit did not trigger at the maximum and minimum peaks of the piezoelectric output voltage and was unreliable. Therefore, the SSSHI circuit did not perform well with the MFC-PZT piezoelements. The bumps in the MFC-PZT output voltage are due to the increased stiffness of the piezoelement. When the MFC-PZT is adhered to the piezoelement substrate it increases the stiffness of the overall piezoelement compared to that of PVDF. This increased stiffness causes a 'whipping' action of piezoelement when it undergoes it maximum stress points. This in turn causes higher frequency components in the output voltage at the positive and negative peaks.

The output power of the SSSHI circuit was comparable to using a direct discharge method or full-wave rectification. No power data for the MFC-PZT piezoelements under SSSHI has been reported in this thesis because the SSSHI circuit has not given any gains over the conventional full-wave rectifier (only circuit complexity has been gained here!). Future research should facilitate a more appropriately designed piezoelement to accommodate incorporate the stiffness of the MFC-PZT.

The best results to date from a MFC-PZT (d-31 mode) piezoelement (employing a conventional full-wave rectifier) is 2.65mW across an 80kΩ load. This is shown in **Figure 6.16**.

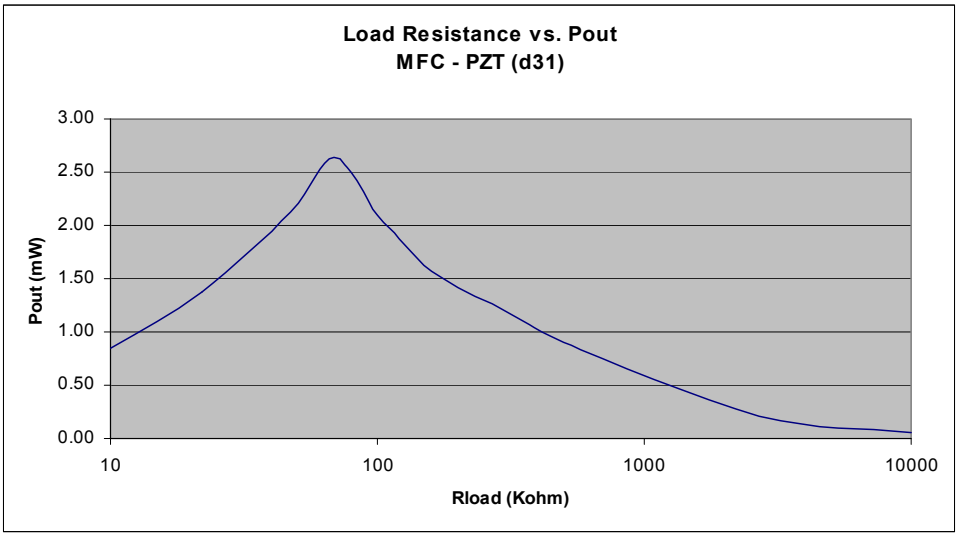

Figure 6.16 *Load resistance versus output power for a MCT-PZT (d-31 mode) piezoelement subjected to a wind speed of 14mph.*

The best results to date for a MFC-PZT (d-33 mode) piezoelement (employing a conventional full-wave rectifier) is 3.1mW across an 800kΩ load. Load resistance versus output power is shown in **Figure 6.17**.

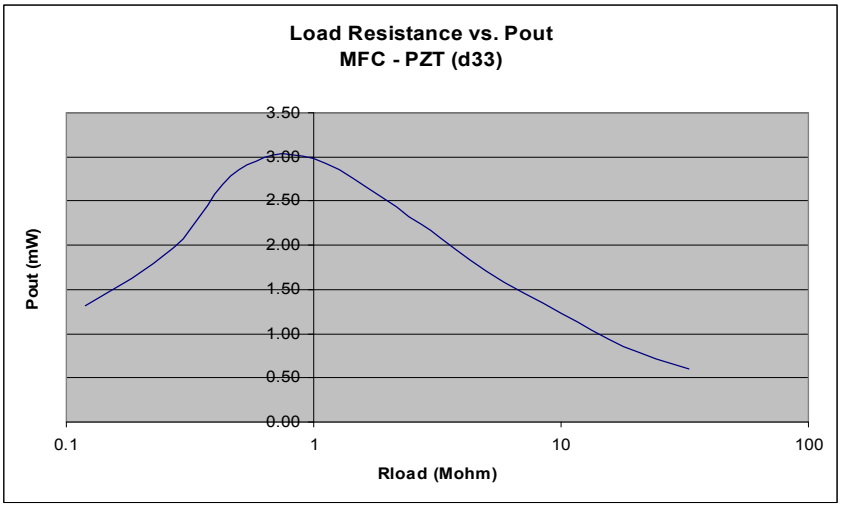

Figure 6.17 *Load resistance versus output power for MFC-PZT (d-33 mode) piezoelements subjected to a wind speed of 14mph.*

MFC-PZT (d33-mode) and MFC-PZT (d31-mode) piezoelectrics were adhered to the same substrate. A photograph of the piezoelement is shown in **Figure 6.18**.

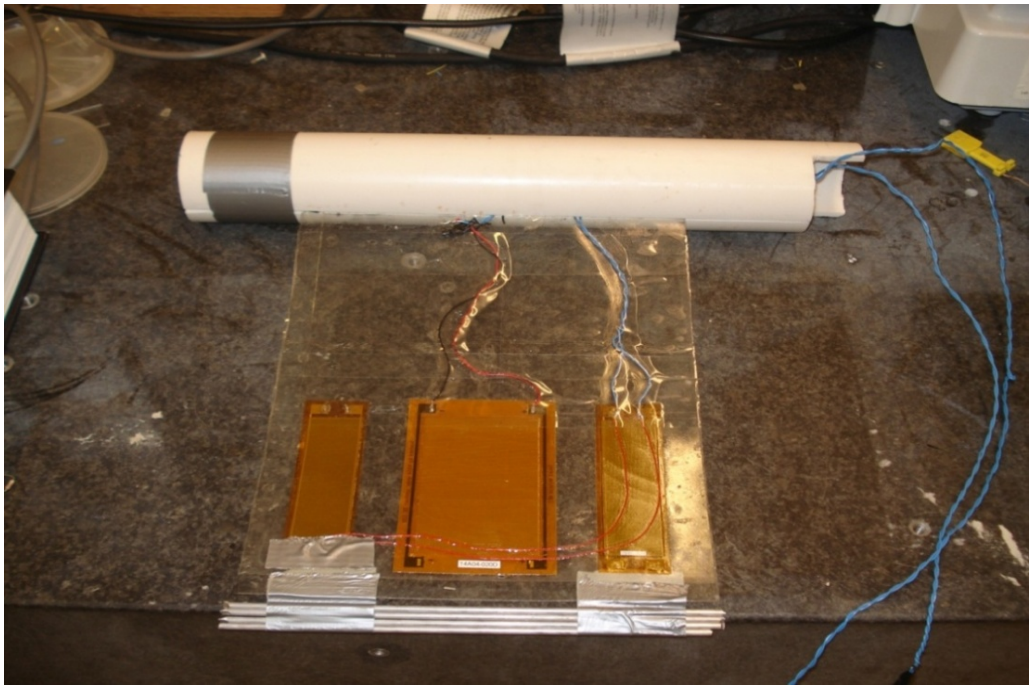

Figure 6.18 *Photograph of MFC-PZT piezoelement. MFC-PZT (d31-mode) is on outer edges of piezoelement and MFC-PZT (d33-mode) is in the middle of the piezoelement.*

The power densities of the MFC-PZT (d31-mode), MFC-PZT (d33-mode), and PVDF were calculated and compared to that of state-of-the-art wind turbines in terms of mW/cm^3. The results are shown in the **Table 6.2**.

Wind Speed ~ 15 mph	**Width (cm)**	**Length (cm)**	**Height (cm)**	**Volume (cm^3)**
MFC-PZT (d33-mode)	21.6	26	13	7300
MFC-PZT (d13mode) 2 pc.	21.6	26	13	7300
PVDF	21.6	26	13	7300
	Pmax (mW)		**PD ($\mu W/cm^3$)**	
PZT (d33)	3.05		0.90	X2 per sheet
PZT (d31)	2.60		0.71	X2 per sheet
PVDF	3.50		0.48	
PVDF - SSSHI	12.00		1.64	
Wind-Turbine (WT)			1.600	
		WT/PZT		**WT/PVDF(SSSHI)**
Power Density Ratio		1780		975

Table 6.2 *Geometric dimensions of MFC-PZT (d31-mode), MFC-PZT (d33-mode) and PVDF. Also, power density calculation results are shown and compared to state-of-the-art wind turbine power densities at a wind speed of 15mph.*

PVDF and MFC-PZT have been shown to give power densities much less than that of wind turbines; thus, mass power generation by piezoelements under wind flow does not seem feasible at this time.

6.3 Fatigue Testing

The following section will discuss the lifetime of the piezoelement. Initial fatigue testing was done using a PVDF bimorph at a wind speed of 14mph. This particular Piezo element was constructed of transparency films glued together by a 3M spray adhesive. The bimorph dimensions are 5" x 7" x .019". The bimorph was placed horizontally in the wind tunnel and ran for periods of roughly 3-5 hours per day for two weeks. The fatigue testing wind speed is 14mph. Output voltages measured are across 500kΩ load utilizing the SSSHI circuit. **Figure 6.19** shows the degradation of the bimorph voltage and capacitance as number of the number of cycles increase. The many bumps in the graph are due to the piezoelectric recovering between periods of testing.

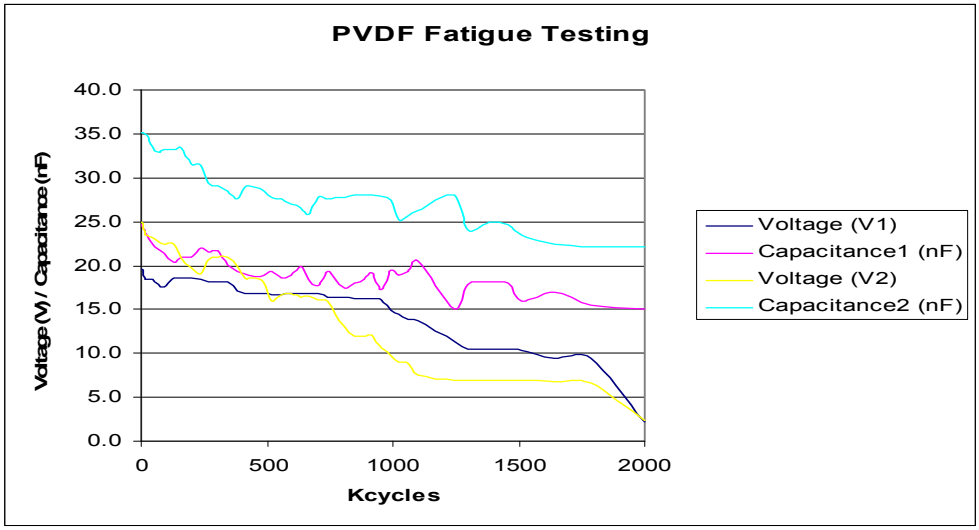

Figure 6.19 *PVDF fatigue testing with 3M spray adhesive used to construct bimorph*

The dissipation factor or the inverse of the Q value of the PVDF was also measured during the fatigue testing since the performance of the SSSHI circuit is highly dependent on the Q value of the LC resonance. The increasing dissipation factor $(\text{Q value})^{-1}$ of the PVDF is displayed in **Figure 6.20**. Again, the bumps in the graph are due to the piezoelectric recovering between testing cycles.

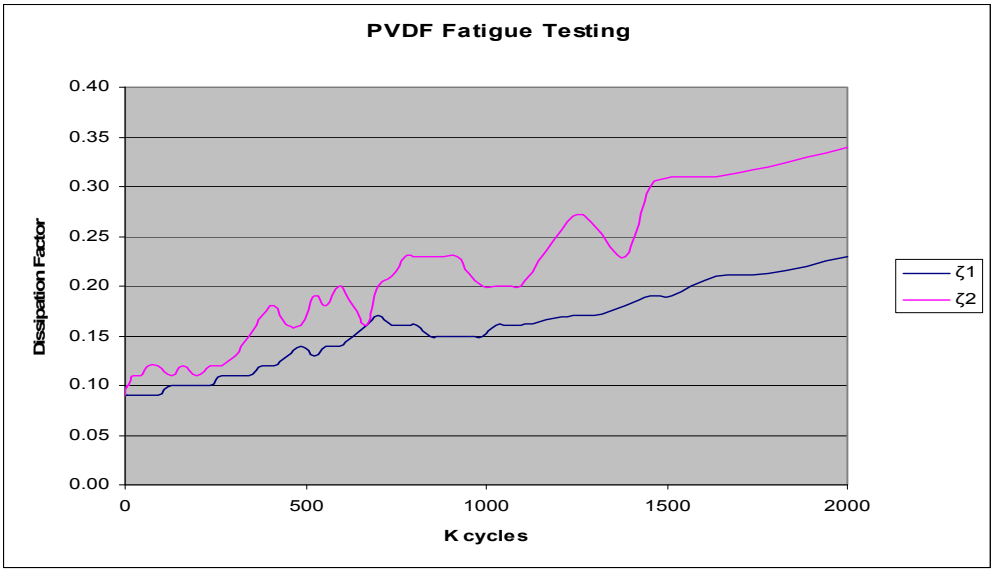

Figure 6.20 *PVDF fatigue testing with 3M spray adhesive used to construct bimorph*

This degradation of the PVDF bimorph performance was due to the spray-on adhesive used to bond the mechanical structure together. The 3M spray on adhesive could be having a chemical reaction with the PVDF, thus degrading the piezoelectricity. This problem was rectified by using a 3M tape adhesive 200MP. With the new tape adhesive the piezoelement held together much better than the piezoelement bonded together with the 3M spray-on adhesive. Another bimorph of the same dimensions was constructed using the 3M tape adhesive. A graph showing the fatigue testing results of the improved piezoelement is shown in **Figure 6.21**.

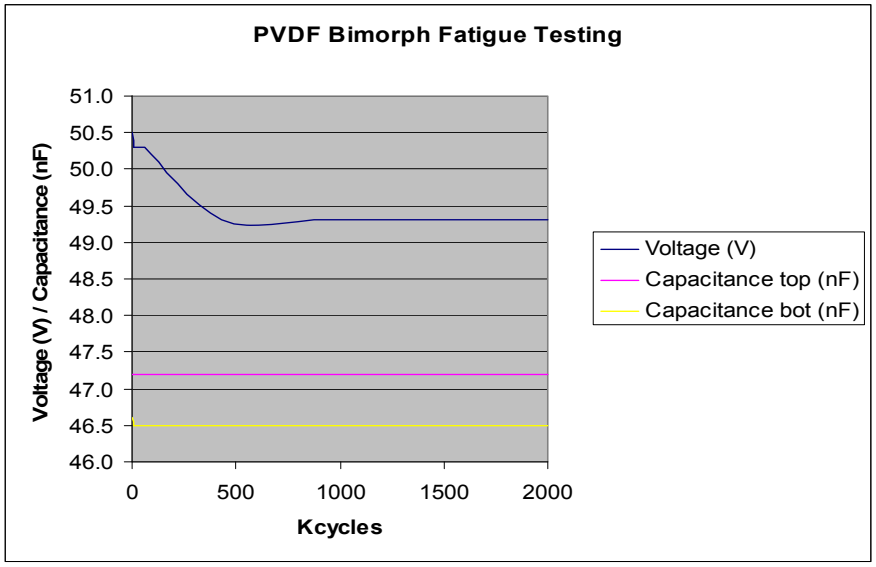

Figure 6.21 *PVDF fatigue testing up to 2 million cycles with 3M tape adhesive used to construct bimorph.*

There is very little degradation of the PVDF output voltage or PVDF capacitance after 2 million cycles and one can safely assume that the structure will remain intact for much longer periods of time. More importantly, the dissipation factor of both pieces of PVDF ($\delta = .02$) does not increase under long periods of alternating stress. This makes the whole concept of harvesting wind energy via piezoelectric materials very attractive, since the SSSHI circuit will continually increase the electrical conversion efficiency by a factor of 3-4 due to the low dissipation factor of the piezoelectric.

CHAPTER 7

Future Work

Although much work has been done in this thesis research to increase the wind to electrical energy conversion efficiency of piezoelements, there is more room for improvement. Yet to be explored, is stacking multiple pieces of PVDF on each outer layer of the piezoelement. This would in fact increase the overall thickness of the piezoelement and thus decrease its flexibility, but it would undoubtedly increase the output power given per piezoelement. This in turn would dramatically increase the overall efficiency of the wind kinetic energy to electrical energy conversion of the piezo element.

Another topic which needs further exploration is the geometry of the piezoelement itself. Yes, stacking of piezoelements could result in much higher output powers, but the 5mil thick 3M tape adhesive used in this research would not be a good candidate for this kind of multiple stacked piezoelement design. A 1mil adhesive would need to be used to give a good ratio of PVDF to adhesive. Stated again for convenience, the PVDF thickness is 70μm (~3mils).

The use of bluff bodies to increase undulation of the piezoelement was explored on a very limited basis in this research. This should be a main topic of further research. Achieving vortex shedding and bimorph mechanical oscillation frequency coupling could greatly increase the kinetic energy to elastic energy conversion efficiency.

Multiple bimorphs could be co-located to achieve more power. The synchronization of multiple elements must be explored. This would facilitate the use of one set of power conditioning electronics for multiple bimorphs.

The SSSHI circuitry shall be optimized to power a real electronic load such as battery charging or powering a wireless sensor.

Switch capacitance and inductor resonance after switch opening should be further investigated. This could be another source for excess power dissipation.

Additional circuitry could be added to extract small amounts of power from the piezoelement under conditions when there isn't enough energy to activate the SSSHI.

REFERENCES

[1] George W. Taylor, Joseph R. Burns, Sean M. Kammann, William B. Powers, Thomas R. Welsh, *The Energy Harvesting Eel: A Small Subsurface Ocean/River Power Generator*, IEEE Journal of Oceanic Engineering, Vol. 20, No.4, Oct. 2001, p. 539-547.

[2] J.J. Allen, A.J. Smits, *Energy Harvesting Eel*, Dept. of Mechanical and Aerospace, Princeton University, 16 November 2000.

[3] V. Hugo Schmidt, *Piezoelectric Energy Conversion in Windmills*, Physics Dept., Montana State University, IEEE Ultrasonics Symposium, 1992, p.897-904

[4] Geffrey K. Ottman, Heath F. Hoffman, Archin C. Bhatt, George A. Lesieutre, *Adaptive Piezoelectric Energy Harvesting circuit for Wireless Remote Power Supply*, IEEE Transactions on Power Electronics, Vol.17, No5, Sept. 2002

[5] William P. Robbins, Ivan Marusic, Dustin Morris, Todd Novak. "Wind-Generated Electrical Energy Using Flexible Piezoelectric Materials". IMECE2006-14050.

[6] Steven R. Anton and Henry A. Sodano. "A Review of Power Harvesting Using Piezoelectric Materials (2003-2006)". May 2007.

[7] Richard Cass, Farhad Mohammadi, Steve Leschin. *A Novel Power Source for Powering Wireless Sensor Networks, Embedded and Other Electronic Systems Using Ambient Energy, Harvested By Piezoelectric Fiber Composites, Eliminating Batteries. 2004*

[8] Chang Bun Yoon, Sung Mi Lee, Hyoun Ee Kim, Kyoung-Woo Lee. *Sensors and Actuators A: Physical*. Vol. 134, Issue 2, 15 March 2007, Pages 519-524

[9] Shashank Priya, Chih-Ta Chen, Darren Fye, and Jeff Zahnd. *Piezoelectric Windmill: A Novel Solution to Remote Sensing*. Japanese Journal of Applied Physics. Vol. 44, No.3, 2005, pp. 104–107.

[10] Smart Material. <http://www.smart-material.com/media/Publications/MFCdata%2013-3-web.pdf>. Sept. 11, 2006

[11] Gyuhae Park. "Overview of Energy Harvesting Systems". Los Alamos National Laboratory. http://www.lanl.gov/projects/ei/pdf_files/Overview%20of%20energy%20harvesting%20systemsLA-UR_8296.pdf. 2006

APPENDIX A –PIEZO OPEN-CIRCUIT VOLTAGE AND MAXIMUM OUTPUT POWER

The electric displacement D_3 for the piezo element shown in Fig. 13 is given by

$$D_3 = \varepsilon_{33} E_3 + d_{31}\sigma_1 \tag{A1}$$

Where σ_1 is the tensile stress indicated in Fig. 13. The strain in the x_1 direction, σ_1, is given by

$$\delta_1 = d_{13} E_3 + Y^{-1}\sigma_1 \tag{A2}$$

Where Y is Young's modulus. With no purposely applied external voltage, $E_3 = 0$, and D_3, using Eq. (A2) becomes

$$D_3(x_1) = d_{13} Y \delta_1(x_1) \tag{A3}$$

Under open circuit conditions, this D_3 will induce a charge Q on the upper and lower electrodes of the piezo element which is given by

$$Q = W \int_0^L D_3(x_1)dx_1 = W \int_0^L d_{13} Y \delta(x_1)dx_1 \tag{A4}$$

The charge Q is related to the open-circuit voltage by

$$Q = C_s V_{oc} = \frac{\varepsilon_{ss} LW}{T} V_{oc} \tag{A5}$$

Solving Eq. (A5) for V_{oc} and using Eq. (A4) for Q yields

$$V_{oc} = \frac{d_{13} Y T}{\varepsilon_{33} L} \int_0^L \delta(x_1) dx_1 \qquad \text{(A6)}$$

Eq. (A6), or equivalently Eq. (4) of the main text, can be used to estimate V_{oc} if the strain $y(x_1)$ is known. This strain can be estimated using Eq. (A7)

$$\delta(x) \approx \frac{T}{2 \frac{d^2}{dx_1^2} (y(x_1))} \qquad \text{(A7)}$$

where 'T' is the radius of curvature [5]. The second derivative of the displacement $y(x_1)$ is obtained by fitting a continuous (and hence differentiable) function to the measured piezo element displacement data such as shown in Fig. 6, and then using numerical techniques to obtain the second derivative.

If the voltage generated by a flapping piezo element is full-wave rectified, the maximum dc power delivered to the load is, using Eq. (7), given by

$$P_{\max} = \frac{V_s^2}{4 R_s} \qquad \text{(A8)}$$

With R_s given by Eq. (5). The source capacitance C_s is given by

$$C_s = \frac{\varepsilon_{33} L W}{T} \qquad \text{(A9)}$$

The source resistance R_s, using Eq. (A9) and using $T_s = 1/f_s$, can be expressed as

$$R_s = \frac{T}{4 f_s \varepsilon_{33} LW} \tag{A10}$$

Equating V_s to V_{oc}, given by Eq. (A6) and for simplicity assuming a spatially-independent strain δ in Eq. (A6), the expression for P_{max} becomes

$$P_{max} = \frac{(d_{13} Y)^2}{\varepsilon_{33}} f_s (LWT) \delta^2 \tag{A11}$$

APPENDIX B – EFFECTIVE SOURCE RESISTANCE SSSHI

Under these conditions, the current i(t) is given by

$$i(t) \approx A\exp(-t/\tau)\sin(\omega_R t) \qquad \text{(B1)}$$

Where $\tau = 2L/(R)$, $\omega_R = \omega_o\sqrt{1-(2Q_s)^{-2}}$, $\omega_o = (LC_s)^{-1/2}$ and $Q_s = \omega_o L/R$. The charge Q_{ex} extracted from the piezo element during this interval is

$$Q_{ex} = \int_0^{\pi/\omega_o} i(t)dt = \frac{A}{\omega_o}(1+e^{-\phi})\sqrt{1-\frac{1}{4Q_s^2}} \qquad \text{(B2)}$$

Where $\varphi = \pi / (2Q_s)$. The charge Q_{ex} replaces the charge drained from the storage capacitor C during the time interval $T_s/2$ ($T_s = 1/f_s$ where f_s is the frequency of the flapping of the piezo element). The charge drawn from the storage capacitor is approximately given by

$$Q_{ex} = \frac{V_o T_s}{2R_L} \qquad \text{(B3)}$$

And the constant 'A' in Eqs. (B1) and (B2) becomes

$$A = \frac{V_o T_s \omega_o}{2R_L(1+e^{-\phi})\sqrt{1-\frac{1}{4Q_s^2}}} \qquad \text{(B4)}$$

During the time interval $T_{cl} \approx \pi/\omega_o$, the energy E_s extracted from the piezo element is given by B5.

$$E_s = V_s Q_{ex} = \frac{V_s V_o T_s}{2R_L} \tag{B5}$$

This extracted energy is balanced by energy dissipation and energy storage in the rest of the circuit. Conservation of energy considerations yields

$$E_s = E_R + E_C \tag{B6}$$

Where E_R is the energy dissipated in the inductor parasitic series resistance R (and on-state resistance of the switch) during the T_{cl}, and E_C is the energy stored in the capacitor C and then dissipated in the load between re-charging intervals.

The energy E_C is given by

$$E_C = \frac{V_o^2 T_s}{2R_L} \tag{B7}$$

The energy E_R dissipated in the resistor R is given by

$$E_R = \int_0^{\pi/\omega_o} Ri^2(t)dt = \frac{V_o^2 T_s^2 (1 - e^{-\phi})}{8C_s R_L^2 (1 + e^{-\phi})} \tag{B8}$$

Using Eqs. (B5), (B7), (A-8) and (B8), the conservation of energy equation, Eq. (B6) becomes

$$\frac{V_s V_o T_s}{2R_L} = \frac{V_o^2 T_s^2 (1 - e^{-\phi})}{8 C_s R_L^2 (1 + e^{-\phi})} + \frac{V_o^2 T_s}{2R_L} \tag{B9}$$

Simplifying Eq. (B9) yields

$$V_o = \frac{V_s}{(1 + R_s / R_L)} \tag{B10}$$

R_S is given by

$$R_s = \frac{T_s}{4C_s}\left[\frac{1 - e^{-\phi}}{1 + e^{-\phi}}\right] \tag{B11}$$

This derivation is essentially the same as published previously [4].